Chapter 15
Friction and Wear on the Atomic Scale

Enrico Gnecco, Roland Bennewitz, Oliver Pfeiffer, Anisoara Socoliuc, and Ernst Meyer

Abstract Friction has long been the subject of research: the empirical da Vinci–Amontons friction laws have been common knowledge for centuries. Macroscopic experiments performed by the school of *Bowden* and *Tabor* revealed that macroscopic friction can be related to the collective action of small asperities. Over the last 15 years, experiments performed with the atomic force microscope have provided new insights into the physics of single asperities sliding over surfaces. This development, together with the results from complementary experiments using surface force apparatus and the quartz microbalance, have led to the new field of *nanotribology*. At the same time, increasing computing power has permitted the simulation of processes that occur during sliding contact involving several hundreds of atoms. It has become clear that atomic processes cannot be neglected when interpreting nanotribology experiments. Even on well-defined surfaces, experiments have revealed that atomic structure is directly linked to friction force. This chapter will describe friction force microscopy experiments that reveal, more or less directly, atomic processes during sliding contact.

We will begin by introducing friction force microscopy, including the calibration of cantilever force sensors and special aspects of the ultrahigh vacuum environment. The empirical Tomlinson model often used to describe atomic stick-slip results is therefore presented in detail. We review experimental results regarding atomic friction, including thermal activation, velocity dependence and temperature dependence. The geometry of the contact is crucial to the interpretation of experimental results, such as the calculation of the lateral contact stiffness, as we shall see. The onset of wear on the atomic scale has recently been studied experimentally and it is described here. In order to compare results, we present molecular dynamics simulations that are directly related to atomic friction experiments. The chapter ends with a discussion of dissipation measurements performed in noncontact force microscopy, which may become an important complementary tool for the study of mechanical dissipation in nanoscopic devices.

B. Bhushan (ed.), *Nanotribology and Nanomechanics*,
DOI 10.1007/978-3-642-15263-4_15,

15.1 Friction Force Microscopy in Ultrahigh Vacuum

The *friction force microscope* (FFM, also called the lateral force microscope, LFM) exploits the interaction of a sharp tip sliding on a surface in order to quantify dissipative processes down to the atomic scale (Fig. 15.1).

15.1.1 Friction Force Microscopy

The relative motion of tip and surface is realized by a *scanner* created from piezoelectric elements, which moves the surface perpendicularly to the tip with a certain periodicity. The scanner can be also extended or retracted in order to vary the normal force F_N that is applied to the surface. This force is responsible for the deflection of the *cantilever* that supports the tip. If the normal force F_N increases while scanning due to the local slope of the surface, the scanner is retracted by a feedback loop. On the other hand, if F_N decreases, the surface is brought closer to the tip by extending the scanner. In this way, the surface topography can be determined line-by-line from the vertical displacement of the scanner. Accurate control of such vertical movement is made possible by a light beam reflected from the rear of the lever into a photodetector. When the cantilever bends, the light spot on the detector moves up or down and causes the photocurrent to vary, when in turn triggers a corresponding change in the normal force F_N applied.

The relative sliding of tip and surface is usually also accompanied by *friction*. A lateral force F_L, which acts in the opposite direction to the scan velocity v hinders

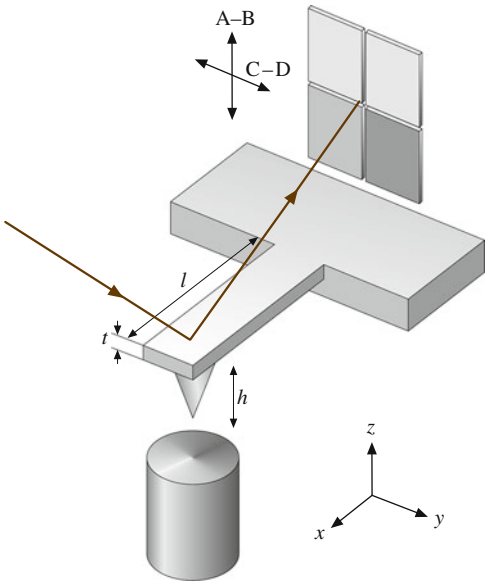

Fig. 15.1 Schematic diagram of a beam-deflection friction force microscope

the motion of the tip. This force causes torsion in the cantilever, which can be observed along with the topography if the photodetector can detect not only the normal deflection but also the lateral movement of the lever while scanning. In practice this is achieved using a four-quadrant photodetectors, as shown in Fig. 15.1. We should note that friction forces also cause lateral bending of the cantilever, but this effect is negligible if the thickness of the lever is much less than the width.

The FFM was first used by Mate et al. in 1987 to study the friction associated with atomic features [1] (just one year after Binnig et al. introduced the atomic force microscope [2]). In their experiment, Mate used a tungsten wire and a slightly different technique to that described above to detect lateral forces (nonfiber interferometry). Optical beam deflection was introduced later by Marti et al. and Meyer et al. [3, 4]. Other methods of measuring the forces between tip and surface include capacitance detection [5], dual fiber interferometry [6] and piezolevers [7]. In the first method, two plates close to the cantilever reveal the capacitance while scanning. The second technique uses two optical fibers to detect the cantilever deflection along two orthogonal directions aligned 45° with respect to the surface normal. Finally, in the third method, cantilevers with two Wheatstone bridges at their bases reveal normal and lateral forces, which are respectively proportional to the sum and the difference of both bridge signals.

15.1.2 Force Calibration

Force calibration is relatively simple if rectangular cantilevers are used. Due to possible discrepancies with the geometric values provided by manufacturers, one should use optical and electron microscopes to determine the width, thickness and length of the cantilever (w, t, l), the tip height h and the position of the tip with respect to the cantilever. The thickness of the cantilever can also be determined from the resonance frequency of the lever f_0 using the relation [8]

$$t = \frac{2\sqrt{12}\pi}{1.875^2}\sqrt{\frac{\rho}{E}}f_0 l^2. \tag{15.1}$$

Here ρ is the density of the cantilever and E is its Young's modulus. The normal spring constant (c_N) and the lateral spring constant (c_L) of the lever are given by

$$c_N = \frac{Ewt^3}{4l^3}, \quad c_L = \frac{Gwt^3}{3h^2 l}, \tag{15.2}$$

where G is the shear modulus. Figure 15.2 shows some SEM images of rectangular silicon cantilevers used for FFM. In the case of silicon, $\rho = 2.33 \times 10^3$ kg/m^3, $E = 1.69 \times 10^{11}$ N/m^2 and $G = 0.5 \times 10^{11}$ N/m^2. Thus, for the cantilever shown in Fig. 15.2, $c_N = 1.9$ N/m and $c_L = 675$ N/m.

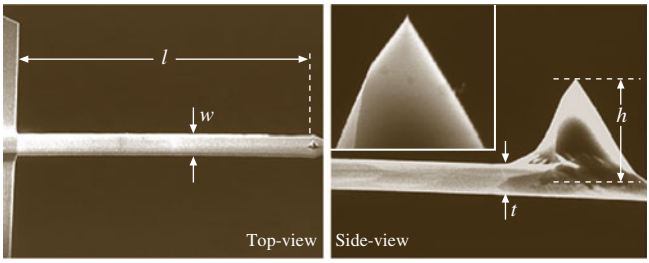

Fig. 15.2 SEM images of a rectangular cantilever. The relevant dimensions are $l = 445$ μm, $w = 43$ μm, $t = 4.5$ μm, $h = 14.75$ μm. Note that h is given by the sum of the tip height and half of the cantilever thickness (after [9])

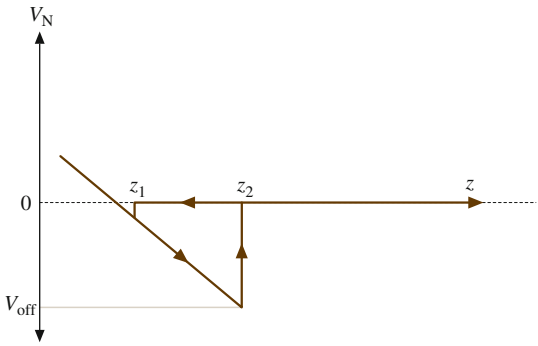

Fig. 15.3 Sketch of a typical force versus distance curve

The next force calibration step consists of measuring the sensitivity of the photodetector S_z (nm/V). For beam-deflection FFMs, the sensitivity S_z can be determined by force versus distance curves measured on hard surfaces (such as Al_2O_3), where elastic deformations are negligible and the vertical movement of the scanner equals the deflection of the cantilever. A typical relation between the difference between the vertical signals on the four-quadrant detector V_N and the distance from the surface (z) is sketched in Fig. 15.3. When the tip is approached, no signal is revealed until the tip jumps into contact at $z = z_1$. Further extension or retraction of the scanner results in elastic behavior until the tip jumps out of contact again at a distance $z_2 > z_1$. The slope of the elastic part of the curve gives the required sensitivity S_z.

The normal and lateral forces are related to the voltage V_N, and the difference between the horizontal signals V_L as follows

$$F_N = c_N S_z V_N, \quad F_L = \frac{3}{2} c_L \frac{h}{l} S_z V_L. \tag{15.3}$$

It is assumed here that the light beam is positioned above the probing tip.

The normal spring constant c_N can also be calibrated using other methods. Cleveland et al. [10] attached tungsten spheres to the tip, which changes the resonance frequency f_0 according to the formula

$$f_0 = \frac{1}{2\pi}\sqrt{\frac{c_N}{M + m^*}}. \tag{15.4}$$

M is the mass of the added object, and m^* is an effective mass of the cantilever, which depends on its geometry [10]. The spring constant can be extrapolated from the frequency shifts corresponding to the different masses attached.

As an alternative, Hutter et al. observed that the spring constant c_N can be related to the area of the power spectrum of the thermal fluctuations of the cantilever P [11]. The correct relation is $c_N = 4k_BT/(3P)$, where $k_B \approx 1.38 \times 10^{-23}$ J/K is Boltzmann's constant and T is the temperature [12].

Cantilevers with different shapes require finite element analysis, although analytical formulas can be derived in a few cases. For V-shaped cantilevers, Neumeister et al. derived the following approximation for the lateral spring constant c_L [13]

$$c_L = \frac{Et^3}{3(1+\nu)h^2} \times \left(\frac{1}{\tan\alpha}\ln\frac{w}{d\sin\alpha} + \frac{L\cos\alpha}{w} - \frac{3\sin 2\alpha}{8}\right)^{-1}. \tag{15.5}$$

The geometrical quantities L, w, α, d, t and h are defined in Fig. 15.4. The expression for the normal constant is more complex and can be found in the cited reference.

Surfaces with well-defined profiles permit an alternative in situ calibration of lateral forces [14]. We present a slightly modified version of the method [15]. Figure 15.5 shows a commercial grating formed by alternate faces with opposite inclinations with respect to the scan direction. When the tip slides on the inclined

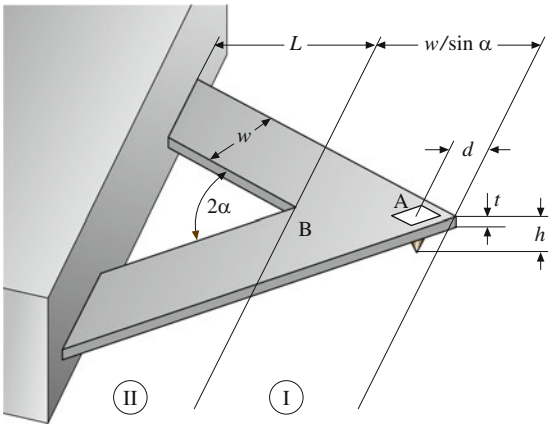

Fig. 15.4 Geometry of a V-shaped cantilever (after [13])

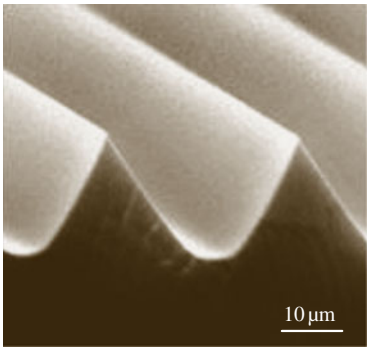

Fig. 15.5 Silicon grating formed by alternated faces angled at ± 55° from the surface (© Silicon-MDT Ltd., Moscow)

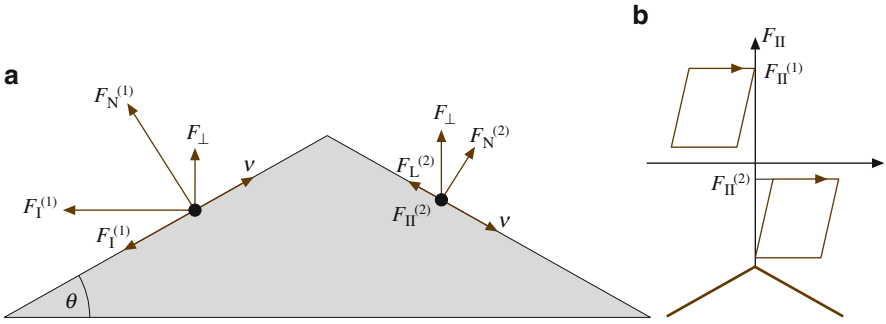

Fig. 15.6 **(a)** Forces acting on a FFM tip sliding on the grating shown in Fig. 15.5; **(b)** friction loops acquired on the two faces

planes, the normal force F_N and the lateral force F_L with respect to the surface are different from the two components $F_\perp$ and $F_\parallel$, which are separated by the photodiode (Fig. 15.6a).

If the linear relation $F_L = \mu F_N$ holds (Sect. 15.5), the component $F_\parallel$ can be expressed in terms of $F_\perp$

$$F_\parallel = \frac{\mu + \tan\theta}{1 - \mu\tan\theta} F_\perp. \tag{15.6}$$

The component $F_\perp$ is kept constant by the feedback loop. The sum of and the difference between the $F_\parallel$ values for the two planes (1) and (2) are given by

$$\begin{aligned} F_+ &\equiv F_\parallel^{(1)} + F_\parallel^{(2)} = \frac{2\mu(1+\tan^2\theta)}{1-\mu^2\tan^2\theta} F_\perp, \\ F_- &\equiv F_\parallel^{(1)} - F_\parallel^{(2)} = \frac{2(1+\mu^2)\tan\theta}{1-\mu^2\tan^2\theta} F_\perp. \end{aligned} \tag{15.7}$$

The values of F_+ and F_- (in volts) can be measured by scanning the profile back and forth (Fig. 15.6b). If F_+ and F_- are recorded with different values of $F_\perp$, one can determine the conversion ratio between volts and nanonewtons as well as the coefficient of friction μ.

An accurate error analysis of lateral force calibration was provided by Schwarz et al., who revealed the importance of the cantilever oscillations induced by the feedback loop and the so-called *pull-off force* (Sect. 15.5) in friction measurements, aside from the geometrical positioning of the cantilevers and laser beams [16]. Other sources of error (in-plane deformation and cantilever tilt) have been recently discussed by Sader and coworkers [17, 18].

An adequate estimation of the radius of curvature of the tip R is also important for some applications (Sect. 15.5.2). This quantity can be evaluated with a scanning electron microscope. This allows well-defined structures such as step sites [19, 20] or whiskers [21] to be imaged. Images of these high aspect ratio structures are convolutions with the tip structure. A deconvolution algorithm that allows for the extraction of the probe tip's radius of curvature was suggested by Villarrubia [22].

15.1.3 The Ultrahigh Vacuum Environment

Atomic friction studies require well-defined surfaces and – whenever possible – tips. For the surfaces, established methods of surface science performed in ultra-high vacuum (UHV) can be employed. Ionic crystals such as NaCl have become standard materials for friction force microscopy on the atomic scale. Atomically clean and flat surfaces can be prepared by cleavage in UHV. The crystal has to be heated to $\approx$150°C for 1 h in order to remove charge after the cleavage process. Metal surfaces can be cleaned and flattened by cycles of sputtering with argon ions and annealing. Even surfaces prepared in air or liquids, such as self-assembled molecular monolayers, can be transferred into the vacuum and studied after careful heating procedures that remove water layers.

Tip preparation in UHV is more difficult. Most force sensors for friction studies have silicon nitride or pure silicon tips. Tips can be cleaned and oxide layers removed by sputtering with argon ions. However, the sharpness of the tip is normally reduced by sputtering. As an alternative, tips can be etched in fluoric acid directly before transfer to the UHV. The significance of tip preparation is limited by the fact that the chemical and geometrical structure of the tip can undergo significant changes when sliding over the surface.

Using the friction force microscope in UHV conditions requires some additional effort. First of all, only materials with low vapor pressures can be used, which excludes most plastics and lubricants. Beam-deflection force microscopes employ either a light source in the vacuum chamber or an optical fiber guiding the light into the chamber. The positioning of the light beam on the cantilever and the reflected beam on the position-sensitive detector is achieved by motorized mirrors [23] or

by moving the light source or detector [24]. Furthermore, a motorized sample approach must be realized.

The quality of the force sensor's electrical signal can seriously deteriorate when it is transferred out of the vacuum chamber. Low noise and high bandwidth can be preserved using a preamplifier in the vacuum. Again, the choice of materials for printing and devices is limited by the need for low vapor pressure. Stronger heating of the electrical circuitry in vacuum, therefore, may be needed.

15.1.4 A Typical Microscope Operated in UHV

A typical AFM used in UHV is shown in Fig. 15.7. The housing (1) contains the light source and a set of lenses that focus the light onto the cantilever. Alternatively, the light can be guided via an optical fiber into the vacuum. By using light emitting diodes with low coherency it is possible to avoid interference effects often found in instruments that use a laser as the light source. A plane mirror fixed on the spherical rotor of a first stepping motor (2) can be rotated around vertical and horizontal axes in order to guide the light beam onto the rear of the cantilever, which is mounted on a removable carrier plate (3). The light is reflected off the cantilever toward a second motorized mirror (4) that guides the beam to the center of the quadrant photodiode (5), where the light is then converted into four photocurrents. Four preamplifiers in close vicinity to the photodiode allow low-noise measurements with a bandwidth of 3 MHz.

The two motors with spherical rotors, used to realign the light path after the cantilever has been exchanged, work as *inertial stepping motors*: the sphere rests on

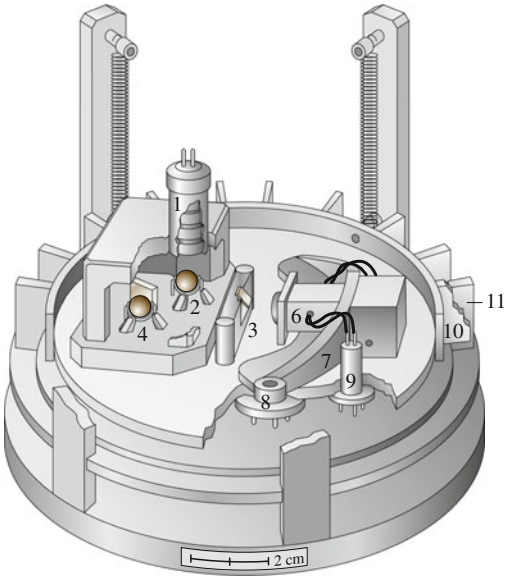

Fig. 15.7 Schematic view of the UHV-AVM realized at the University of Basel (after [23]) (1 – light source, 2, 4 – mirrors, 3 – cantilever holders, 5 – photodetector, 6 – scanner, 7 – slider, 8 – driving piezo, 9 – fixed post, 10, 11 – eddy current damping)

three piezoelectric legs that can be moved in small amounts tangentially to the sphere. Each step of the motor consists of the slow forward motion of two legs followed by an abrupt jump backwards. During the slow forward motion, the sphere follows the legs due to friction, whereas it cannot follow the sudden jump due to its inertia. A series of these tiny steps rotates the sphere macroscopically.

The sample, which is also placed on an exchangeable carrier plate, is mounted at the end of a tube scanner (6), which can move the sample in three dimensions over several micrometers. The whole scanning head (7) is the slider of a third inertial stepping motor for coarse positioning of the sample. It rests with its flat and polished bottom on three supports. Two of them are symmetrically placed piezoelectric legs (8), whereas the third central support is passive. The slider (7) can be moved in two dimensions and rotated about a vertical axis by several millimeters (rotation is achieved by antiparallel operation of the two legs). The slider is held down by two magnets, close to the active supports, and its travel is limited by two fixed posts (9) that also serve as cable attachments. The whole platform is suspended by four springs. A ring of radial copper lamellae (10), floating between a ring of permanent magnets (11) on the base flange, acts to efficiently damp eddy currents.

15.2 The Tomlinson Model

In Sect. 15.3, we show that the FFM can reveal friction forces down to the atomic scale, which are characterized by a typical sawtooth pattern. This phenomenon can be seen as a consequence of a *stick–slip* mechanism, discussed by Tomlinson in 1929 [25].

15.2.1 One-Dimensional Tomlinson Model

In the Tomlinson model, the motion of the tip is influenced by both the interaction with the atomic lattice of the surface and the elastic deformations of the cantilever. The shape of the tip–surface potential $V(\boldsymbol{r})$ depends on several factors, such as the chemical composition of the materials in contact and the atomic arrangement at the tip end. For the sake of simplicity, we will start the analysis in the one-dimensional case considering a sinusoidal profile with an atomic lattice periodicity a and a peak-to-peak amplitude E_0. In Sect. 15.5, we will show how the elasticity of the cantilever and the contact area can be described in a unique framework by introducing an effective lateral spring constant k_{eff}. If the cantilever moves with a constant velocity v along the x-direction, the total energy of the system is

$$E_{\text{tot}}(x,t) = -\frac{E_0}{2}\cos\frac{2\pi x}{a} + \frac{1}{2}k_{\text{eff}}(vt - x)^2. \tag{15.8}$$

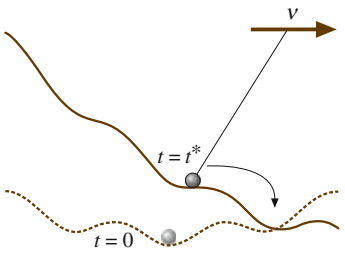

Fig. 15.8 Energy profile experienced by the FFM tip (*black circle*) at $t = 0$ (*dotted line*) and $t = t^*$ (*continuous line*)

Figure 15.8 shows the energy profile $E_{\text{tot}}(x, t)$ at two different instants. When $t = 0$, the tip is localized in the absolute minimum of E_{tot}. This minimum increases with time due to the cantilever motion, until the tip position becomes unstable when $t = t^*$.

At a given time t, the position of the tip can be determined by equating the first derivative of $E_{\text{tot}}(x, t)$ with respect to x to zero

$$\frac{\partial E_{\text{tot}}}{\partial x} = \frac{\pi E_0}{a} \sin \frac{2\pi x}{a} - k_{\text{eff}}(vt - x) = 0. \tag{15.9}$$

The critical position x^* corresponding to $t = t^*$ is determined by equating the second derivative $\partial^2 E_{\text{tot}}(x, t)/\partial x^2$ to zero, which gives

$$x^* = \frac{a}{4} \arccos\left(-\frac{1}{\gamma}\right), \quad \gamma = \frac{2\pi^2 E_0}{k_{\text{eff}} a^2}. \tag{15.10}$$

The coefficient γ compares the strength of the interaction between the tip and the surface with the stiffness of the system. When $t = t^*$ the tip suddenly *jumps* into the next minimum of the potential profile. The lateral force $F^* = k_{\text{eff}}(vt - x^*)$ that induces the jump can be evaluated from (15.9) and (15.10)

$$F^* = \frac{k_{\text{eff}} a}{2\pi} \sqrt{\gamma^2 - 1}. \tag{15.11}$$

Thus the stick–slip is observed only if $\gamma > 1$: when the system is not too stiff or when the tip–surface interaction is strong enough. Figure 15.9 shows the lateral force F_{L} as a function of the cantilever position X. When the cantilever is moved to the right, the lower part of the curve in Fig. 15.9 is obtained. If, at a certain point, the cantilever's direction of motion is suddenly inverted, the force has the profile shown in the upper part of the curve. The area of the *friction loop* obtained by scanning back and forth gives the total energy dissipated.

On the other hand, when $\gamma < 1$, the stick–slip is suppressed. The tip slides in a continuous way on the surface and the lateral force oscillates between negative

and positive values. Instabilities vanish in this regime, which leads to the disappearance of lateral force hysteresis and correspondingly negligible dissipation losses.

15.2.2 Two-Dimensional Tomlinson Model

In two dimensions, the energy of our system is given by

$$E_{\mathrm{tot}}(\boldsymbol{r},t) = U(\boldsymbol{r}) + \frac{k_{\mathrm{eff}}}{2}(\boldsymbol{vt} - \boldsymbol{r})^2, \tag{15.12}$$

where $\boldsymbol{r} \equiv (x, y)$ and $\boldsymbol{v}$ is arbitrarily oriented on the surface (note that $\boldsymbol{v} \neq \mathrm{d}\boldsymbol{r}/\mathrm{d}t$!). Figure 15.10 shows the total energy corresponding to a periodic potential of the form

$$U(x,y,t) = -\frac{E_0}{2}\left(\cos\frac{2\pi x}{a} + \cos\frac{2\pi y}{a}\right) + E_1 \cos\frac{2\pi x}{a}\cos\frac{2\pi y}{a}. \tag{15.13}$$

The equilibrium condition becomes

$$\nabla E_{\mathrm{tot}}(\boldsymbol{r},t) = \nabla U(\boldsymbol{r}) + k_{\mathrm{eff}}(\boldsymbol{r} - \boldsymbol{vt}) = 0. \tag{15.14}$$

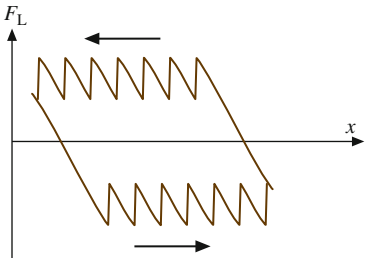

Fig. 15.9 Friction loop obtained by scanning back and forth in the 1-D Tomlinson model. The effective spring constant k_{eff} is the slope of the sticking part of the loop (if $\gamma \gg 1$)

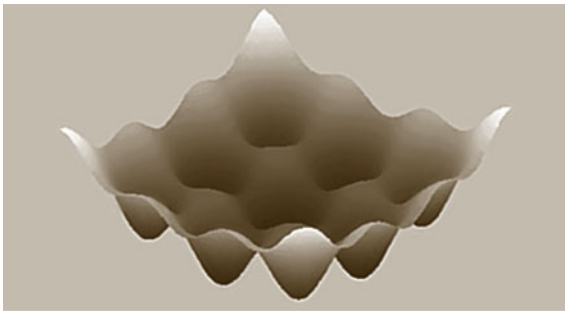

Fig. 15.10 Energy landscape experienced by the FFM tip in 2-D

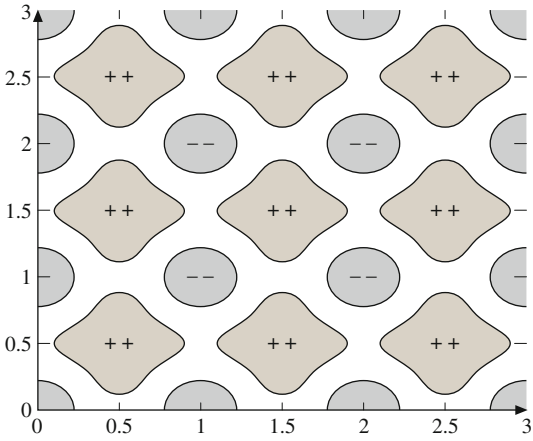

Fig. 15.11 Regions on the tip plane labeled according to the signs of the eigenvalues of the Hessian matrix (after [26])

The stability of the equilibrium can be described by introducing the Hessian matrix

$$H = \begin{pmatrix} \dfrac{\partial^2 U}{\partial x^2} + k_{\text{eff}} & \dfrac{\partial^2 U}{\partial x \partial y} \\ \dfrac{\partial^2 U}{\partial y \partial x} & \dfrac{\partial^2 U}{\partial y^2} + k_{\text{eff}} \end{pmatrix}. \tag{15.15}$$

When both eigenvalues $\lambda_{1,2}$ of the Hessian are positive, the position of the tip is stable. Figure 15.11 shows these regions for a potential of the form (15.13). The tip follows the cantilever adiabatically as long as it remains in the (++)-region. When the tip is dragged to the border of the region, it suddenly jumps into the next (++)-region. A comparison between a theoretical friction map deduced from the 2-D Tomlinson model and an experimental map acquired by UHV-FFM is given in the next section.

15.2.3 Friction Between Atomically Flat Surfaces

So far we have implicitly assumed that the tip is terminated by only one atom. It is also instructive to consider the case of a periodic surface sliding on another periodic surface. In the Frenkel–Kontorova–Tomlinson (FKT) model, the atoms of one surface are harmonically coupled with their nearest neighbors. We will restrict ourselves to the case of quadratic symmetries, with lattice constants a_1 and a_2 for the upper and lower surfaces, respectively (Fig. 15.12). In this context, the role of *commensurability* is essential. It is well known that any real number z can be represented as a continued fraction

$$z = N_0 + \cfrac{1}{N_1 + \frac{1}{N_2 + \ldots}}. \tag{15.16}$$

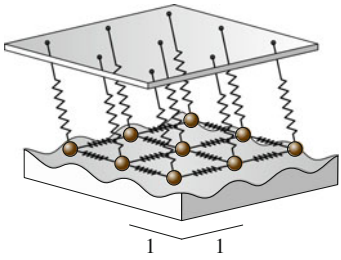

Fig. 15.12 The FKT model in 2-D (after [27])

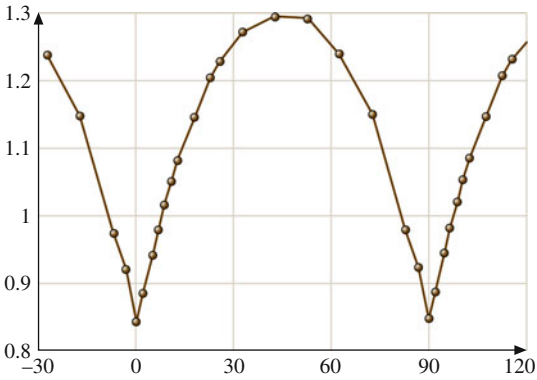

Fig. 15.13 Friction as a function of the sliding angle φ in the 2-D FKT model (after [27])

The sequence that converges most slowly is obtained when all $N_i = 1$, which corresponds to the *golden mean* $\bar{z} = (\sqrt{5} - 1)/2$. In 1-D, Weiss and Elmer predicted that friction should decrease with decreasing commensurability, the minimum friction being reached when $a_1/a_2 = \bar{z}$ [28].

In 2-D, Gyalog and Thomas studied the case $a_1 = a_2$, with a misalignment between the two lattices given by an angle θ [27]. When the sliding direction changes, friction also varies from a minimum value (corresponding to the sliding angle $\varphi = \theta/2$) to a maximum value (which is reached when $\varphi = \theta/2 + \pi/4$; see Fig. 15.13). The misfit angle θ is related to the commensurability. Since the misfit angles that give rise to commensurate structure form a dense subset, the dependence of friction on θ should be discontinuous. The numerical simulations performed by Gyalog are in agreement with this conclusion. The role of intrabulk elastic forces has been considered in a scaling study by Müser [29], where the symmetry of the surfaces and the dimensionalities of interface and solids have been found to play a crucial role.

15.3 Friction Experiments on the Atomic Scale

Figure 15.14 shows the first atomic-scale friction map, as observed by Mate. The periodicity of the lateral force is the same as that of the atomic lattice of graphite. The series of friction loops in Fig. 15.15 reveals the stick–slip effect discussed in

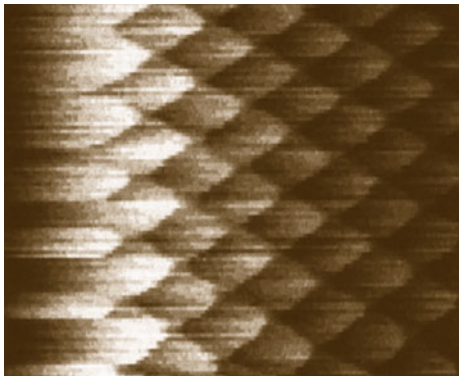

Fig. 15.14 First atomic friction map acquired on graphite with a normal force $F_N = 56$ μN. Frame size: 2 nm (after [1])

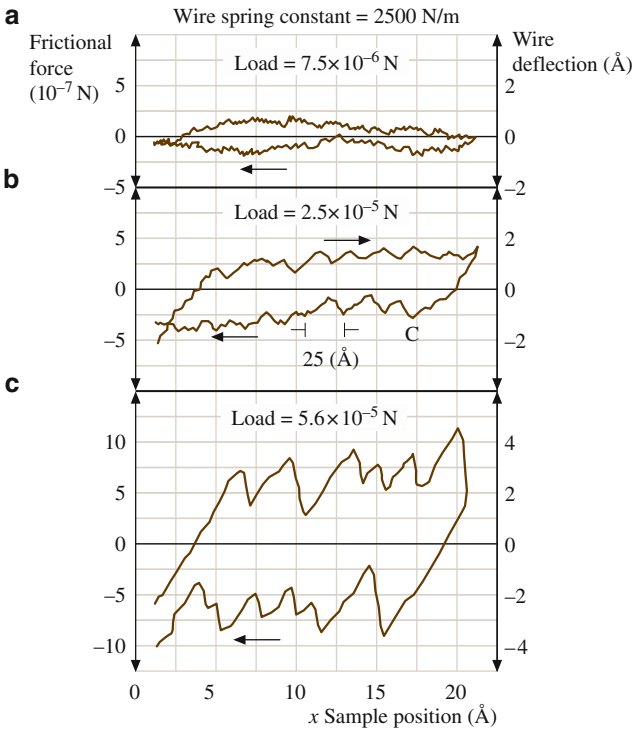

Fig. 15.15 Friction loops on graphite acquired with **(a)** $F_N = 7.5$ μN, **(b)** 24 μN and **(c)** 75 μN (after [1])

the previous section. The applied loads are in the range of tens of μN. According to the continuum models discussed in Sect. 15.5, these values correspond to contact diameters of 100 nm. A possible explanation for the atomic features observed at such high loads is that graphite flakes may have detached from the surface and adhered to the tip [30]. Another explanation is that the contact between tip and

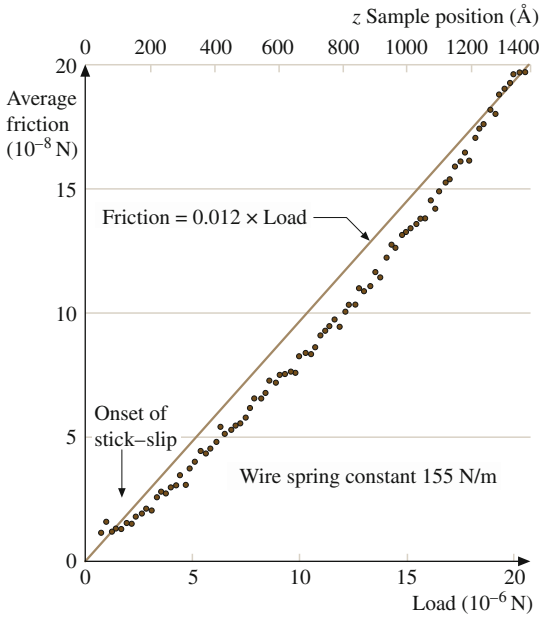

Fig. 15.16 Load dependence of friction on graphite (after [1])

surface consisted of few nm-scale asperities and that the corrugation was not entirely averaged out while sliding. The load dependence of friction as found by Mate is rather linear, with a small friction coefficient $\mu = 0.01$ (Fig. 15.16).

The UHV environment reduces the influence of contaminants on the surface and leads to more precise and reproducible results. Meyer et al. [31] obtained a series of interesting results on ionic crystals using the UHV-FFM apparatus described in Sect. 15.1.4. By applying subnanonewton loads to a NaCl surface, Socoliuc et al. observed the transition from stick–slip to continuous sliding discussed in Sect. 15.2.1 [32]. In another experiment, the same group observed that the transition could also be induced dynamically by superimposed oscillations of the applied load at the contact resonance [33]. In Fig. 15.17, a friction map recorded on KBr(100) is compared with a theoretical map obtained with the 2-D Tomlinson model. The periodicity $a = 0.47$ nm corresponds to the spacing between equally charged ions. No individual defects were observed. One possible reason is that the contact realized by the FFM tip is always formed by many atoms, which superimpose and average their effects. Molecular dynamics (MD) calculations (Sect. 15.7) show that even single-atom contact may cause rather large stresses in the sample, which lead to the motion of defects far away from the contact area. However, this seems to be not the case when ultrathin films of ionic crystals are epitaxially grown on a different species. Indeed, high resolution FFM images of stable defects across a KBr/NaCl interface have been recently reported by Maier and coworkers [35]. The duration of slip events was the main topic of another study on KBr [36]. Here, the broad time distribution experimentally observed was attributed to the atomistic structure of the contact area, in agreement with a multispring model of the tip–surface interface.

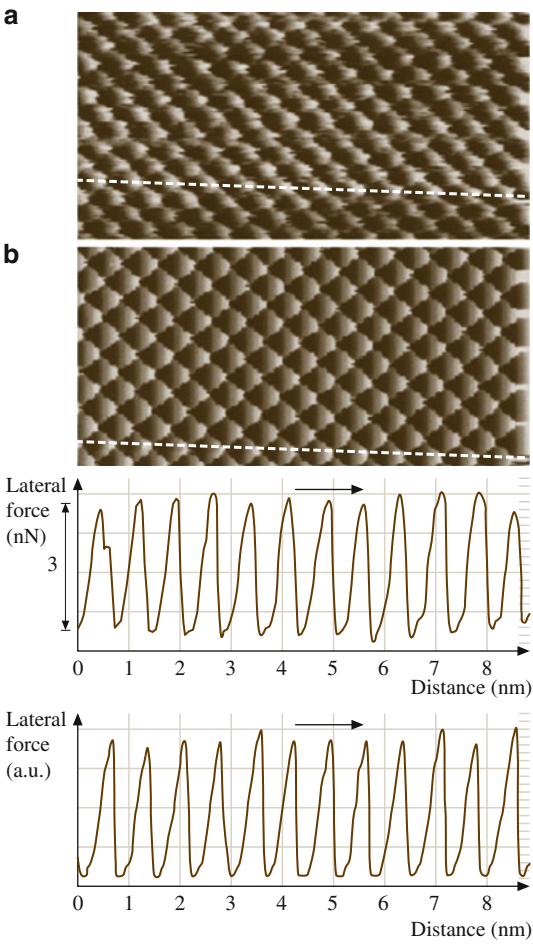

Fig. 15.17 **(a)** Measured and **(b)** theoretical friction map on KBr(100) (after [34])

Lüthi et al. [37] even detected atomic-scale friction on a reconstructed Si(111)-7 $\times$ 7 surface. However, uncoated Si tips and tips coated with Pt, Au, Ag, Cr and Pt/C damaged the sample irreversibly, and the observation of atomic features was achieved only after coating the tips with polytetrafluoroethylene (PTFE), which has lubricant properties and does not react with the dangling bonds of Si(111)-7 $\times$ 7 (Fig. 15.18).

Friction has been resolved on the atomic scale even on metallic surfaces in UHV. In Fig. 15.19 reproducible stick–slip process on Cu(111) is shown. Current measurements performed at the same time suggested that the AFM tip was covered by copper atoms. More recently, the Cu(100) surface has also revealed regular atomic stick–slip [39], despite previous theoretical and experimental observations suggested that the atomic packing of this surface is prone to be worn off by the tip. Sliding on the (100) surface of copper produced irregular patterns, although atomic features were recognized even in this case [38]. Molecular dynamics suggests that

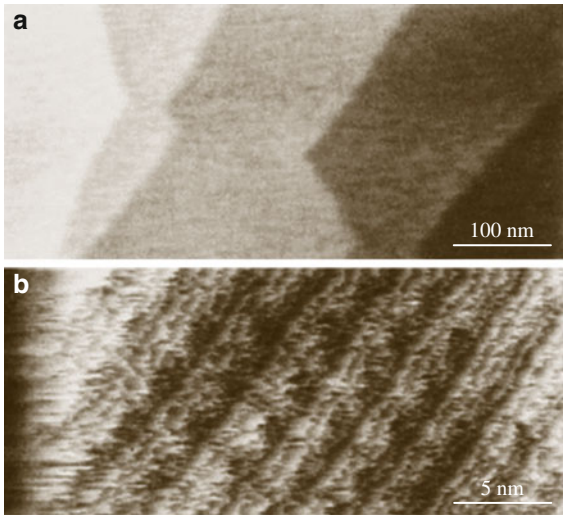

Fig. 15.18 **(a)** Topography and **(b)** friction image of Si(111)7 × 7 measured with a PTFE-coated Si tip (after [37])

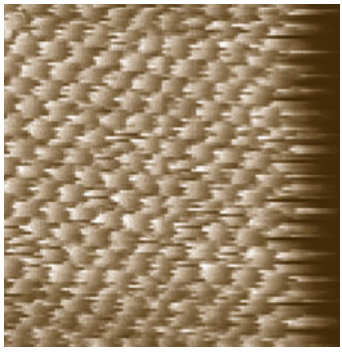

Fig. 15.19 Friction images of Cu(111). Frame size: 3 nm (after [38])

wear should occur more easily on the Cu(100) surface than on the close-packed Cu(111) (Sect. 15.7). This conclusion was achieved by adopting copper tips in computer simulations. The assumption that the FFM tip used in the experiments was covered by copper is supported by current measurements performed at the same time.

Atomic stick–slip on diamond was observed by Germann et al. with an apposite diamond tip prepared by chemical vapor deposition [40] and, a few years later, by van der Oetelaar et al. [41] with standard silicon tips. The values of friction vary dramatically depending on the presence or absence of hydrogen on the surface.

Fujisawa et al. [42] measured friction on mica and on MoS_2 with a 2-D FFM apparatus that could also reveal forces perpendicular to the scan direction. The features in Fig. 15.20 correspond to a zigzag tip walk, which is predicted by the 2-D Tomlinson model [43]. Two-dimensional stick–slip on NaF was detected with normal forces <14 nN, whereas loads of up to 10 μN could be applied to layered materials. The contact between tip and NaF was thus formed by one or a few atoms.

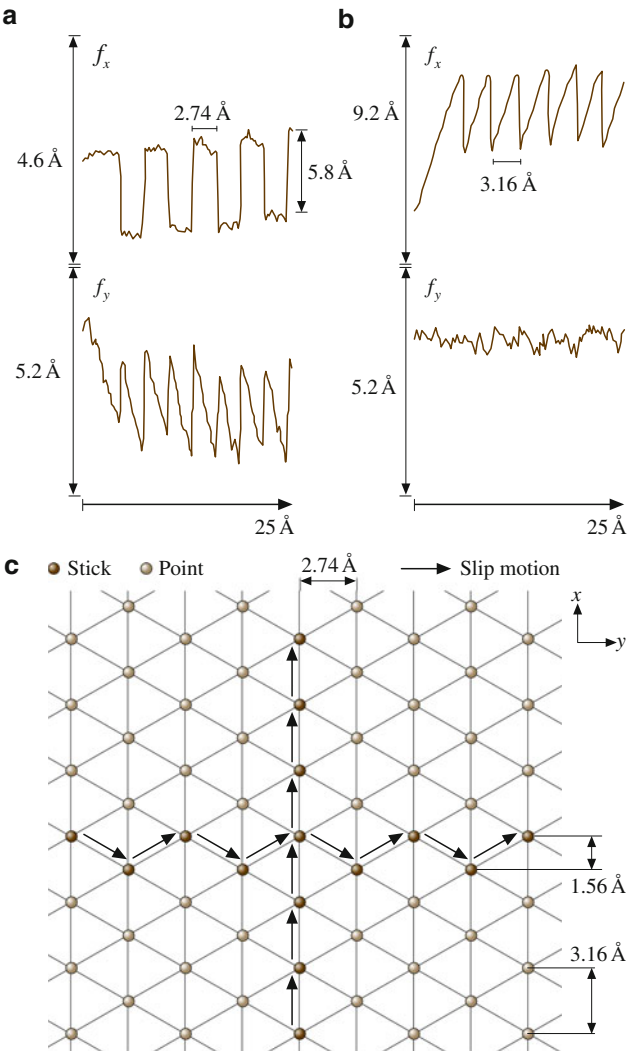

Fig. 15.20 **(a)** Friction force on MoS_2 acquired by scanning along the cantilever and **(b)** across the cantilever. **(c)** Motion of the tip on the sample (after [42])

A zigzag walk on mica was also observed by *Kawakatsu* et al. using an original 2-D FFM with two laser beams and two quadrant photodetectors [44].

15.3.1 Anisotropy of Friction

The importance of the misfit angle in the reciprocal sliding of two flat surfaces was first observed experimentally by Hirano et al. in the contact of two mica sheets [45].

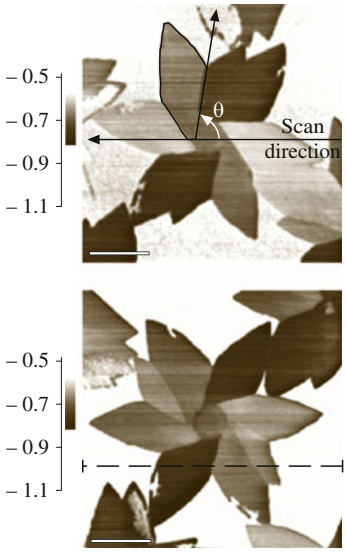

Fig. 15.21 Friction images of a thiolipid monolayer on a mica surface. In **(b)** the sample is rotated by 70° with respect to **(a)** (after [50])

The friction increased when the two surfaces formed commensurate structures, in agreement with the discussion in Sect. 15.2.3. In more recent measurements with a monocrystalline tungsten tip on Si(001), Hirano et al. observed *superlubricity* in the incommensurate case [46].

Overney et al. [47] studied the effects of friction anisotropy on a bilayer lipid film. In this case, different molecular alignments resulted in significant variations in the friction. Other measurements of friction anisotropy on single crystals of stearic acid were reported by Takano and Fujihira [48]. An impressive confirmation of this effect recently came from a dedicated force microscope developed by Frenken and coworkers, the Tribolever, which allows quantitative tracking of the scanning force in three dimensions [49]. With this instrument, a flake from a graphite surface was picked up and the lateral forces between the flake and the surface were measured at different angles of rotation. Stick-slip and energy dissipation were only clearly revealed at rotation angles of 0 and 60°, when the two lattices are in registry.

Liley et al. [50] observed flower-shaped islands of a lipid monolayer on mica, which consisted of domains with different molecular orientations (Fig. 15.21). The angular dependence of friction reflects the tilt direction of the alkyl chains of the monolayer, as revealed by other techniques.

Lüthi et al. [51] used the FFM tip to move C_{60} islands, which slide on sodium chloride in UHV without disruption (Fig. 15.22). In this experiment the friction was found to be independent of the sliding direction. This was not the case in other experiments performed by Sheehan and Lieber, who observed that the misfit angle is relevant when MoO_3 islands are dragged on the MoS_2 surface [52]. In these experiments, sliding was possible only along low index directions. The weak

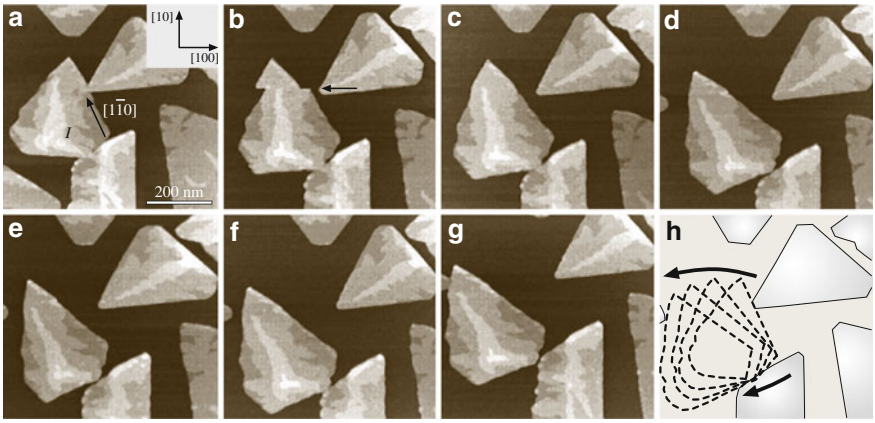

Fig. 15.22 **(a–g)** Sequence of topography images of C_{60} islands on NaCl(100) (after [51]). **(h)** Overview of the roto-translational motion of the island

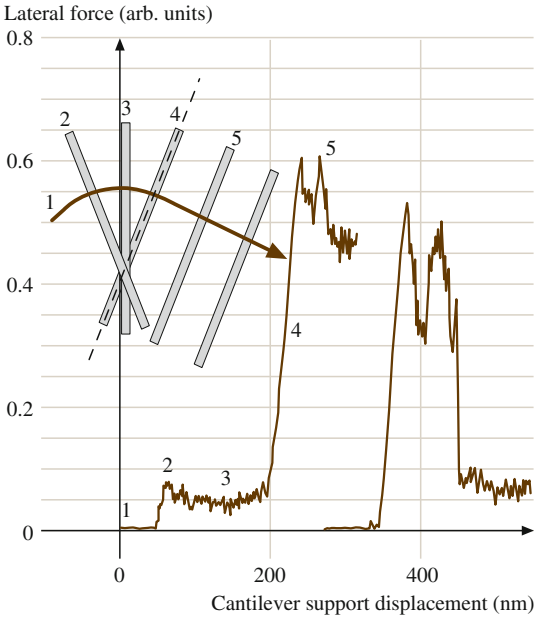

Fig. 15.23 Friction force experienced as a carbon nanotube is rotated into (*left trace*) and out of (*right trace*) commensurate contact (after [53])

orientation dependence found by Lüthi et al. [51] is probably due to the large mismatch of C_{60} on NaCl.

A recent example of friction anisotropy is related to carbon nanotubes. Falvo et al. [53] manipulated nanotubes on graphite using a FFM tip (Fig. 15.23). A dramatic increase in the lateral force was found in directions corresponding to

commensurate contact. At the same time, the nanotube motion changed from sliding/rotating to stick-roll.

15.4 Thermal Effects on Atomic Friction

Although the Tomlinson model gives a good interpretation of the basic mechanism of the atomic stick–slip discussed in Sect. 15.2, it cannot explain some minor features observed in the atomic friction. For example, Fig. 15.24 shows a friction loop acquired on NaCl(100). The peaks in the sawtooth profile have different heights, which is in contrast to the result in Fig. 15.9. Another effect is observed if the scan velocity v is varied: the mean friction force increases with the logarithm of v (Fig. 15.25). This effect cannot be interpreted within the mechanical approach in Sect. 15.2 without further assumptions.

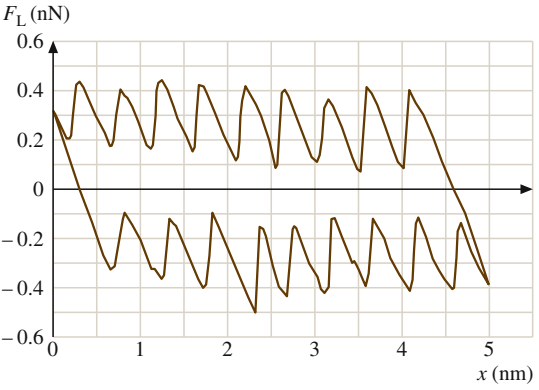

Fig. 15.24 Friction loop on NaCl(100) (after [54])

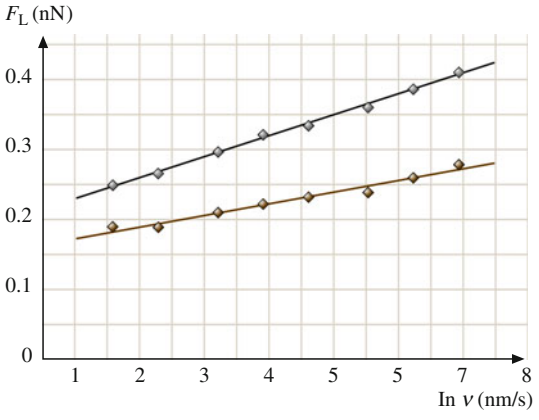

Fig. 15.25 Mean friction force vs. scanning velocity on NaCl(100) at $F_N = 0.44$ nN (+) and $F_N = 0.65$nN (×) (after [54])

15.4.1 The Tomlinson Model at Finite Temperature

Let us focus again on the energy profile discussed in Sect. 15.2.1. For the sake of simplicity, we will assume that $\gamma \gg 1$. At a given time $t < t^*$, the tip jump is prevented by the energy barrier $\Delta E = E(x_{\max}, t) - E(x_{\min}, t)$, where $x_{\max}$ corresponds to the first maximum observed in the energy profile and $x_{\min}$ is the actual position of the tip (Fig. 15.26). The quantity ΔE decreases with time or, equivalently, with the frictional force F_{L} until it vanishes when $F_{\mathrm{L}} = F^*$ (Fig. 15.27). Close to the critical point, the energy barrier can be written approximately as

$$\Delta E = \lambda(\tilde{F} - F_{\mathrm{L}}), \tag{15.17}$$

where $\tilde{F}$ is close to the critical value $F^* = \pi E_0/a$.

At finite temperature T, the lateral force required to induce a jump is lower than F^*. To estimate the most probable value of F_{L} at this point, we first consider the probability p that the tip does *not* jump. The probability p changes with time t according to the master equation

$$\frac{\mathrm{d}p(t)}{\mathrm{d}t} = -f_0 \exp\left(-\frac{\Delta E(t)}{k_{\mathrm{B}}T}\right) p(t), \tag{15.18}$$

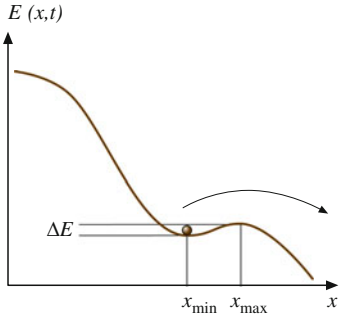

Fig. 15.26 Energy barrier that hinders the tip jump in the Tomlinson model

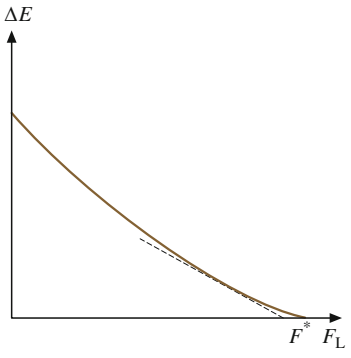

Fig. 15.27 Energy barrier ΔE as a function of the lateral force F_{L}. The *dashed line* close to the critical value corresponds to the linear approximation (15.17)

where f_0 is a characteristic frequency of the system. The physical meaning of this frequency is discussed in Sect. 15.4.2. We should note that the probability of a reverse jump is neglected, since in this case the energy barrier that must be overcome is much higher than ΔE. If time is replaced by the corresponding lateral force, the master equation becomes

$$\frac{\mathrm{d}p(F_\mathrm{L})}{\mathrm{d}F_\mathrm{L}} = -f_0 \exp\left(-\frac{\Delta E(F_\mathrm{L})}{k_\mathrm{B}T}\right)\left(\frac{\mathrm{d}F_\mathrm{L}}{\mathrm{d}t}\right)^{-1} p(F_\mathrm{L}). \tag{15.19}$$

At this point, we substitute

$$\frac{\mathrm{d}F_\mathrm{L}}{\mathrm{d}t} = \frac{\mathrm{d}F_\mathrm{L}}{\mathrm{d}X}\frac{\mathrm{d}X}{\mathrm{d}t} = k_\mathrm{eff} v \tag{15.20}$$

and use the approximation (15.17). The maximum probability transition condition $\mathrm{d}^2p(F)/\mathrm{d}F^2 = 0$ then yields

$$F_\mathrm{L}(v) = F^* - \frac{K_\mathrm{B}T}{\lambda}\ln\frac{v_\mathrm{c}}{v} \tag{15.21}$$

with

$$v_\mathrm{c} = \frac{f_0 k_\mathrm{B} T}{k_\mathrm{eff}\lambda}. \tag{15.22}$$

Thus, the lateral force depends logarithmically on the sliding velocity, as observed experimentally. However, approximation (15.17) does not hold when the tip jump occurs very close to the critical point $x = x^*$, which is the case at high velocities. In this instance, the factor $(\mathrm{d}F_\mathrm{L}\mathrm{d}t)^{-1}$ in (15.19) is small and, consequently, the probability $p(t)$ does not change significantly until it suddenly approaches 1 when $t \to t^*$. Thus friction is constant at high velocities, in agreement with the classical Coulomb's law of friction [31].

Sang et al. [55] observed that the energy barrier close to the critical point is better approximated by a relation like

$$\Delta E = \mu(F^* - F_\mathrm{L})^{3/2}. \tag{15.23}$$

The same analysis performed using approximation (15.23) instead of (15.17) leads to the expression [56]

$$\frac{\mu(F^* - F_\mathrm{L})^{3/2}}{k_\mathrm{B}T} = \ln\frac{v_\mathrm{c}}{v} - \sqrt{1 - \frac{F^*}{F_\mathrm{L}}}, \tag{15.24}$$

where the critical velocity v_c is now

$$v_c = \frac{\pi\sqrt{2}}{2}\frac{f_0 k_B T}{k_{eff} a}. \tag{15.25}$$

The velocity v_c discriminates between two different regimes. If $v \ll v_c$, the second logarithm in (15.24) can be neglected, which leads to the logarithmic dependence

$$F_L(v) = F^* - \left(\frac{k_B T}{\mu}\right)^{2/3}\left(\ln\frac{v_c}{v}\right)^{2/3}. \tag{15.26}$$

In the opposite case, $v \gg v_c$, the term on the left in (15.23) is negligible and

$$F_L(v) = F^*\left[1 - \left(\frac{v_c}{v}\right)^2\right]. \tag{15.27}$$

In such a case, the lateral force F_L tends to F^*, as expected.

In a recent work, Reimann et al. distinguished between the dissipation that occurs in the tip apex and that in the substrate volume in contact with the tip [57]. After the initial logarithmic increase, the velocity dependence of friction changes in different ways, depending on the relative contribution of the tip apex to the total dissipation. A *friction plateau* is only predicted when $\theta \approx 0.5$ over a limited velocity range. At lower or higher values of θ, friction is expected to increase, or, respectively, decrease beyond the critical velocity v_c.

The thermally activated Tomlinson model has been recently extended to two dimensions by Fasolino and coworkers [58].

15.4.2 Velocity Dependence of Friction

The velocity dependence of friction was only recently studied by FFM. Zwörner et al. observed that friction between silicon tips and diamond, graphite or amorphous carbon is constant with scan velocities of a few μm/s [62]. The friction decreased when v was reduced below 1 μm/s. In their experiment on lipid films on mica (Sect. 15.3.1), Gourdon et al. [60] explored a range of velocities from 0.01 to 50 μm/s and found a critical velocity $v_c = 3.5$ μm/s that discriminates between an increasing friction and a constant friction regime (Fig. 15.28). Although these results were not explained by thermal activation, we argue that the previous theoretical discussion gives the correct interpretative key. A clear observation of a logarithmic dependence of friction on the micrometer scale was reported by Bouhacina et al., who studied friction on triethoxysilane molecules and polymers grafted on silica with sliding velocities of up to $v = 300$ μm/s [61]. The result was

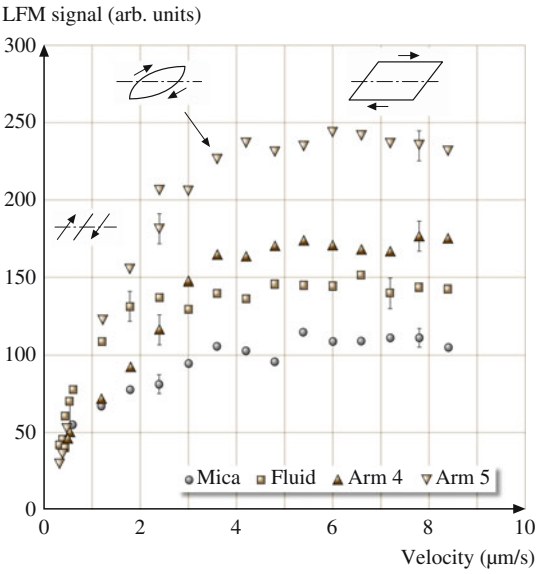

Fig. 15.28 Velocity dependence of friction on mica and on lipid films with different orientations (arms 4 and 5) and in a fluid phase (after [60])

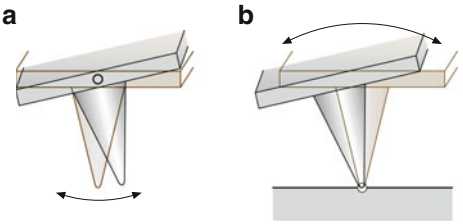

Fig. 15.29 Torsional modes of cantilever oscillation **(a)** when the tip is free and **(b)** when the tip is in contact with a surface (after [65])

explained with a thermally activated Eyring model, which does not differ significantly from the model discussed in the previous subsection [62, 63].

The first measurements on the atomic scale were performed by Bennewitz et al. on copper and sodium chloride [54, 64]; in both cases a logarithmic dependence of friction was revealed up to $v < 1$ μm/s (Fig. 15.25), in agreement with (15.21). Higher values of velocities were not explored, due to the limited range of the scan frequencies possible with FFM on the atomic scale. The same limitation does not allow a clear distinction between (15.21) and (15.26) when interpreting the experimental results.

At this point we would like to discuss the physical meaning of the characteristic frequency f_0. With a lattice constant a of a few angstroms and an effective spring constant $k_{\text{eff}} \approx 1$ N/m, which are typical of FFM experiments, (15.25) gives a value of a few hundred kHz for f_0. This is the characteristic range in which the torsional eigenfrequencies of the cantilevers are located in both contact and noncontact modes (Fig. 15.29). Future work may clarify whether or not f_0 must be identified with these frequencies.

To conclude this section, we should emphasize that the increase in friction with increasing velocity is ultimately related to the materials and the environment in which the measurements are realized. In a humid environment, Riedo et al. observed that the surface wettability plays an important role [66]. Friction *decreases* with increasing velocity on hydrophilic surfaces, and the rate of this decrease depends drastically on humidity. A logarithmic increase is again found on partially hydrophobic surfaces (Fig. 15.30). These results were interpreted

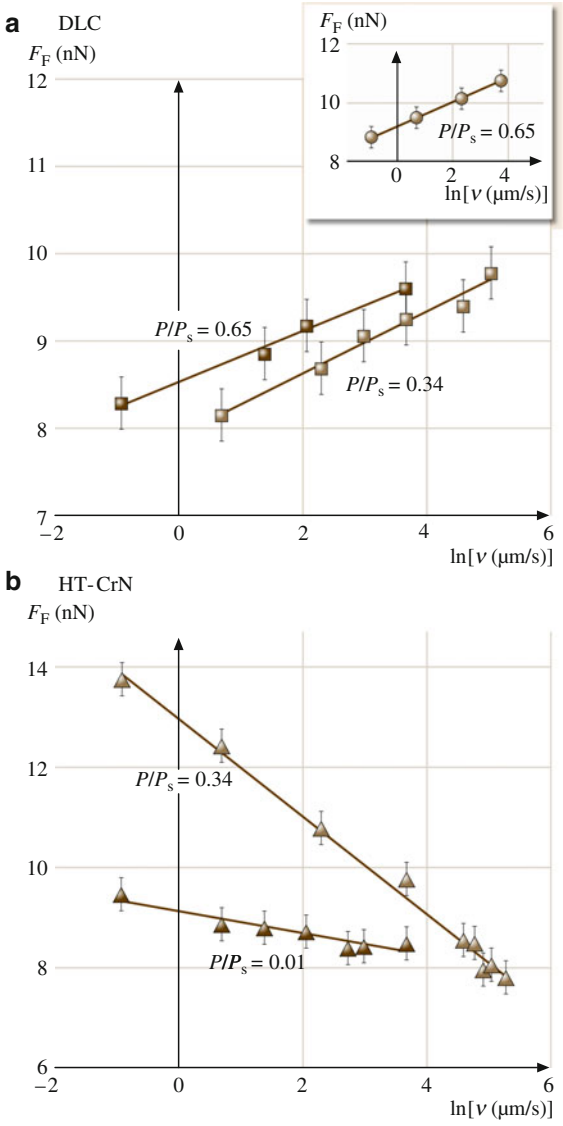

Fig. 15.30 Friction versus sliding velocity **(a)** on hydrophobic surfaces and **(b)** on hydrophilic surfaces (after [66])

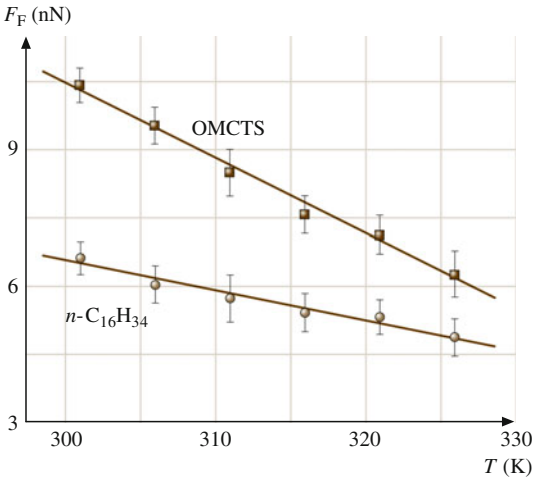

Fig. 15.31 Temperature dependence of friction on *n*-hexadecane and octamethylcyclotetrasiloxane (after [67])

considering the thermally activated nucleation of water bridges between tip and sample asperities, as discussed in the cited reference.

15.4.3 Temperature Dependence of Friction

Thus far we have used thermal activation to explain the velocity dependence of friction. The same mechanism also predicts that friction should change with temperature. The master equation (15.18) shows that the probability of a tip jump is reduced at low temperatures T until it vanishes when $T = 0$. Within this limit case, thermal activation is excluded, and the lateral force F_L is equal to F^*, independent of the scanning velocity v.

Only few experimental studies focused on the temperature dependence of friction, none of them revealing atomic-scale features. A linear decrease of friction with temperature was observed on silicon surfaces covered by organic molecules in a limited range of temperatures [67]. On bare Si(111) in UHV a peak of friction was found ≈100 K, the origin of which remained unexplained [68]. In a recent FFM study on graphite Zhao et al. [69] found a significant dependence of friction on $1/T$ over a wide temperature range (140–750 K), supporting the hypothesis of thermal activation of the stick–slip process.

15.5 Geometry Effects in Nanocontacts

Friction is ultimately related to the real shape of the contact between the sliding surfaces. On the macroscopic scale, the contact between two bodies is studied within the context of continuum mechanics, which is based on the elasticity theory

developed by Hertz in the nineteenth century. Various FFM experiments have shown that continuum mechanics is still valid down to contact areas just a few nanometers in size. Only when contact is reduced to few atoms does the continuum frame become unsuitable, and other approaches like molecular dynamics become necessary. This section will deal with continuum mechanics theory; molecular dynamics will be discussed in Sect. 15.7.

15.5.1 Continuum Mechanics of Single Asperities

The lateral force F_L between two surfaces in reciprocal motion depends on the size of the real area of contact, A, which can be a few orders of magnitude smaller than the apparent area of contact. The simplest assumption is that friction is proportional to A; the proportionality factor is called the *shear strength* σ [70]

$$F_L = \sigma A. \tag{15.28}$$

For plastic deformation, the asperities are compressed until the pressure p equals a certain yield value p^*. The resulting contact area is thus $A = F_N/p^*$, and the well-known Amontons' law is obtained: $F_L = \mu F_N$, where $\mu = \sigma/p^*$ is the *coefficient of friction*. The same idea can be extended to contacts formed by many asperities, and it leads again to Amontons' law. The simplicity of this analysis explains why most friction processes were related to plastic deformation for a long time. Such a mechanism, however, should provoke quick disruption of surfaces, which is not observed in practice.

Elastic deformation can be easily studied in the case of a sphere of radius R pressed against a flat surface. In this case, the contact area is

$$A(F_N) = \pi \left(\frac{R}{K}\right)^{2/3} F_N^{2/3}, \tag{15.29}$$

where $K = 3E^*/4$ and E^* is an effective Young's modulus, related to the Young's moduli (E_1 and E_2) and the Poisson numbers (ν_1 and ν_2) of sphere and plane, by the following relation [71]

$$\frac{1}{E^*} = \frac{1-\nu_1^2}{E_1} + \frac{1-\nu_2^2}{E_2}. \tag{15.30}$$

The result $A \propto F_N^{2/3}$ contrasts with Amontons' law. However, a linear relation between F_L and F_N can be obtained for contacts formed from several asperities in particular cases. For example, the area of contact between a flat surface and a set of asperities with an exponential height distribution and the same radius of curvature R depends linearly on the normal force F_N [72]. The same conclusion holds approximately even for a Gaussian height distribution. However, the hypothesis that the radii of curvature are the same for all asperities is not realistic. A general model was

recently proposed by Persson, who analytically derived the proportionality between contact area and load for a large variety of elastoplastic contacts formed by surfaces with arbitrary roughnesses [73]. However, this discussion is not straightforward and goes beyond the purposes of this section.

Further effects are observed if adhesive forces between the asperities are taken into account. If the range of action of these forces is smaller than the elastic deformation, (15.29) is extended to the Johnson–Kendall–Roberts (JKR) relation

$$A(F_{\mathrm{N}}) = \pi\left(\frac{R}{K}\right)^{2/3} \times \left(F_{\mathrm{N}} + 3\pi\gamma R + \sqrt{6\pi\gamma R F_{\mathrm{N}} + (3\pi\gamma R)^2}\right)^{2/3}, \tag{15.31}$$

where γ is the surface tension of the sphere and plane [74]. The real contact area at zero load is finite and the sphere can be detached only by pulling it away with a certain force. This is also true in the opposite case, in which the range of action of adhesive forces is larger than the elastic deformation. In this case, the relation between contact area and load takes the simple form

$$A(F_{\mathrm{N}}) = \pi\left(\frac{R}{K}\right)^{2/3} (F_{\mathrm{N}} - F_{\mathrm{off}})^{2/3}, \tag{15.32}$$

where F_{off} is the negative load required to break the contact. The Hertz-plus-offset relation (15.32) can be derived from the Derjaguin–Muller–Toporov (DMT) model [75]. To discriminate between the JKR or DMT models, Tabor introduced a nondimensional parameter

$$\Phi = \left(\frac{9R\gamma^2}{4K^2 z_0^3}\right)^{1/3}, \tag{15.33}$$

where z_0 is the equilibrium distance during contact. The JKR model can be applied if $\Phi > 5$; the DMT model holds when $\Phi < 0.1$ [76]. For intermediate values of Φ, the Maugis–Dugdale model [77] could reasonably explain experimental results (Sect. 15.5.3).

15.5.2 Dependence of Friction on Load

The FFM tip represents a single asperity sliding on a surface. The previous discussion suggests a nonlinear dependence of friction on the applied load, provided that continuum mechanics is applicable. Schwarz et al. observed the Hertz-plus-offset relation (15.32) on graphite, diamond, amorphous carbon and C_{60} in an argon atmosphere (Fig. 15.32). In their measurements, they used well-defined spherical tips with radii of curvature of tens of nanometers, obtained by contaminating silicon tips with amorphous carbon in a transmission electron microscope. In order to

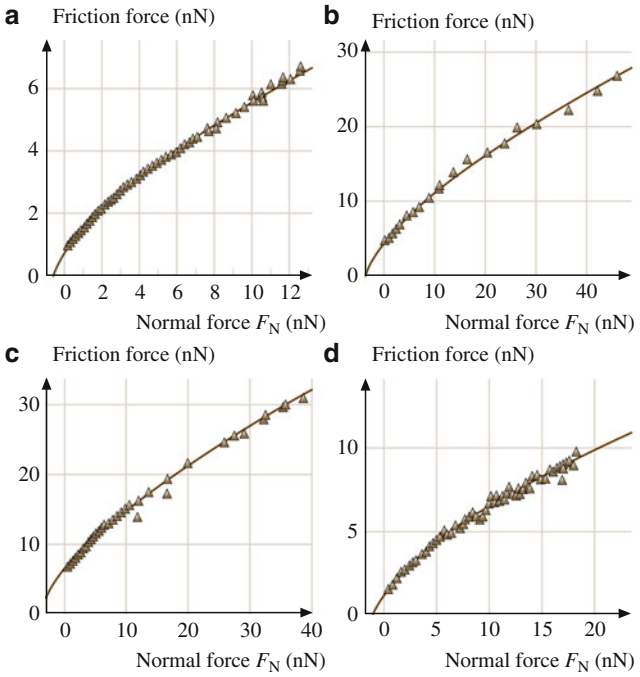

Fig. 15.32 Friction versus load curve on amorphous carbon in argon atmosphere. Curves **(a)–(d)** refer to tips with different radii of curvature (after [78])

compare the tribological behavior of different materials, Schwarz et al. suggested the introduction of an effective coefficient of friction $\tilde{C}$ which is independent of the tip curvature [78].

Meyer et al., Carpick et al., and Polaczyc et al. performed friction measurements in UHV in agreement with JKR theory [19, 79, 80]. Different materials were considered (ionic crystals, mica and metals) in these experiments. In order to correlate the lateral and normal forces with improved statistics, Meyer et al. applied an original 2-D histogram technique (Fig. 15.33). Carpick et al. extended the JKR relation (15.32) to include nonspherical tips. In the case of an axisymmetric tip profile $z \propto r^{2n}$ $(n > 1)$, it can be proven analytically that the increase in the friction becomes less pronounced with increasing n (Fig. 15.34).

15.5.3 Estimation of the Contact Area

In contrast to other tribological instruments, such as the surface force apparatus [81], the contact area cannot be measured directly by FFM. Indirect methods are provided by contact stiffness measurements. The contact between the FFM tip and

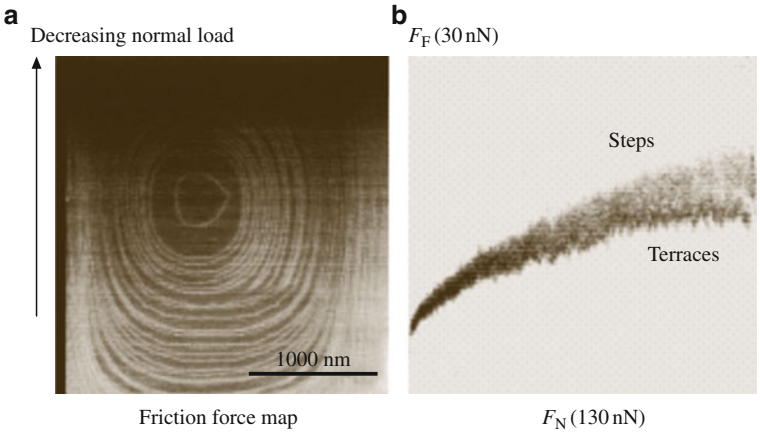

Fig. 15.33 **(a)** Friction force map on NaCl(100). The load is decreased from 140 to 0 nN (jump-off point) during imaging. **(b)** 2-D histogram of **(a)** (after [19])

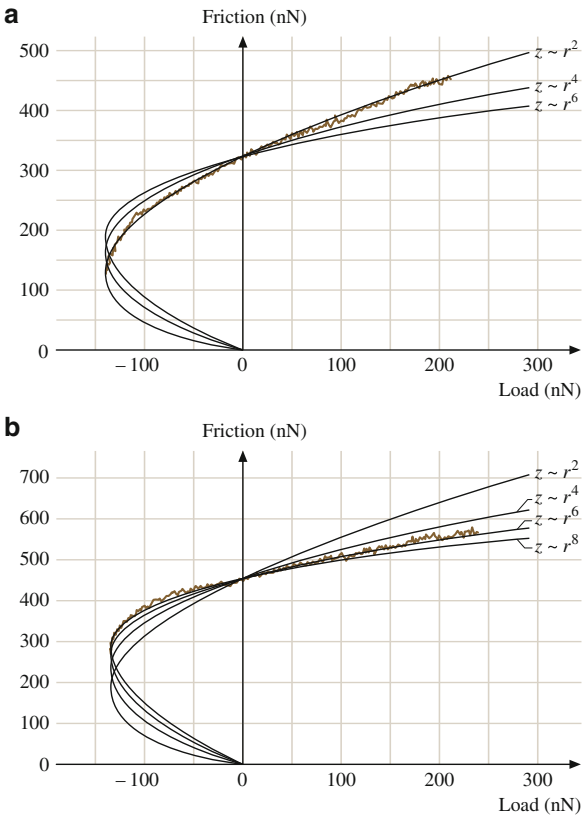

Fig. 15.34 Friction versus load curves **(a)** for a spherical tip and **(b)** for a blunted tip. The *solid curves* are determined using the JKR theory (after [79])

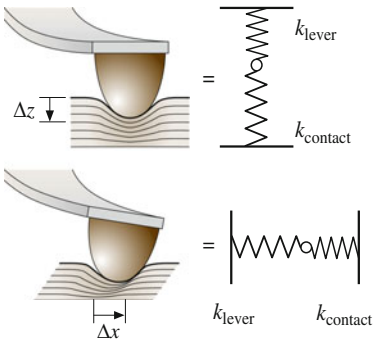

Fig. 15.35 Sketch of normal and lateral stiffness of the contact between tip and surface (after [83])

the sample can be modeled by a series of two springs (Fig. 15.35). The effective constant k^z_{eff} of the series is given by

$$\frac{1}{k^z_{\text{eff}}} = \frac{1}{k^z_{\text{contact}}} + \frac{1}{c_{\text{N}}}, \tag{15.34}$$

where c_{N} is the normal spring constant of the cantilever and k^z_{contact} is the normal stiffness of the contact. This quantity is related to the radius of the contact area (a) by the simple relation

$$k^z_{\text{contact}} = 2aE^*, \tag{15.35}$$

where E^* is the effective Young's modulus introduced previously [82]. Typical values of k^z_{contact} are an order of magnitude larger than c_{N}, however, and practical application of (15.34) is not possible.

Carpick et al. independently suggested an alternative method [83, 84]. According to various models, the *lateral* contact stiffness of the contact between a sphere and a flat surface is [85]

$$k^x_{\text{contact}} = 8aG^*, \tag{15.36}$$

where the effective shear stress G^* is defined by

$$\frac{1}{G^*} = \frac{2-\nu_1^2}{G_1} + \frac{2-\nu_2^2}{G_2}. \tag{15.37}$$

G_1, G_2 are the shear moduli of the sphere and the plane, respectively. The contact between the FFM tip and the sample can again be modeled by a series of springs (Fig. 15.35). The effective constant k^x_{eff} of the series is given by

$$\frac{1}{k^x_{\text{eff}}} = \frac{1}{k^x_{\text{contact}}} + \frac{1}{k^x_{\text{tip}}} + \frac{1}{c_{\text{L}}}, \tag{15.38}$$

where c_L is the lateral spring constant of the cantilever and $k^x_{contact}$ is the lateral stiffness of the contact. As suggested by Lantz, (15.38) also includes the lateral stiffness of the tip k^x_{tip} which can be comparable to the lateral spring constant. The effective spring constant k^x_{eff} is simply given by the slope dF_L/dx of the friction loop (Sect. 15.2.1). Once $k^x_{contact}$ is determined, the contact radius a is easily estimated by (15.36).

The lateral stiffness method was applied to contacts between silicon nitride and muscovite mica in air and between $NbSe_2$ and graphite in UHV. The dependences of both the spring constant k^x_{eff} and the lateral force F_L on the load F_N were explained within the same models (JKR and Maugis–Dugdale, respectively), which confirms that friction is proportional to the contact area for the range of loads applied (up to $F_N = 40$ nN in both experiments).

Enachescu et al. estimated the contact area by measuring the contact conductance on diamond as a function of the applied load [86, 87]. Their experimental data were fitted with the DMT model, which was also used to explain the dependence of friction on load. Since the contact conductance is proportional to the contact area, the validity of the hypothesis (15.28) was confirmed again.

15.6 Wear on the Atomic Scale

If the normal force F_N applied by the FFM exceeds a critical value, which depends on the tip shape and on the material under investigation, the surface topography is permanently modified. In some cases wear is exploited to create patterns with well-defined shapes. Here we will focus on the mechanisms that act at the nanometer scale, where recent experiments have demonstrated the unique ability of the FFM to both scratch and image surfaces down to the atomic scale.

15.6.1 Abrasive Wear on the Atomic Scale

Lüthi et al. observed the appearance of wear at very low loads, i.e. $F_N = 3$ nN, for ionic crystals [34]. Atomically resolved images of the damage produced by scratching the FFM tip area on potassium bromide were obtained by Gnecco et al. [88]. In Fig. 15.36, a small mound that has piled up at the end of a groove on KBr(100) is shown at different magnifications. The groove was created a few minutes before imaging by repeatedly scanning with the normal force $F_N = 21$ nN. The image shows a lateral force map acquired with a load of $\approx$1 nN; no atomic features were observed in the corresponding topographic signal. Figure 15.36a, b shows that the debris extracted from the groove recrystallized with the same atomic arrangement of the undamaged surface, which suggests that the wear process occurred in a similar way to epitaxial growth, assisted by the microscope tip.

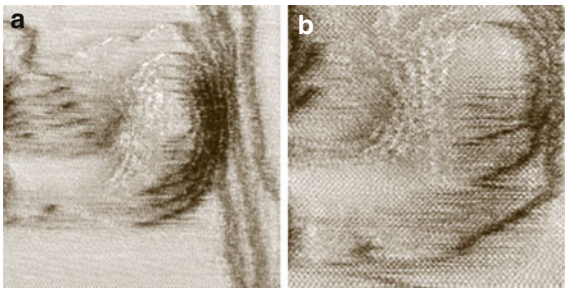

Fig. 15.36 Lateral force images acquired at the end of a groove scratched 256 times with a normal force $F_N = 21$ nN. Frame sizes: **(a)** 39 nm, **(b)** 25 nm

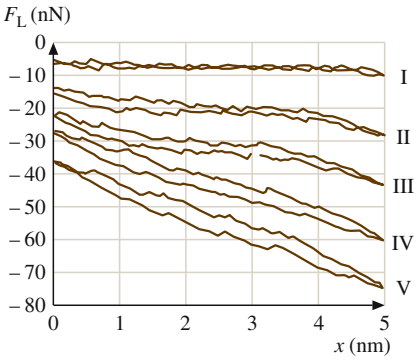

Fig. 15.37 Friction loops acquired while scratching the KBr surface on 5 nm long lines with different loads $F_N = 5.7$–22.8 nN (after [88])

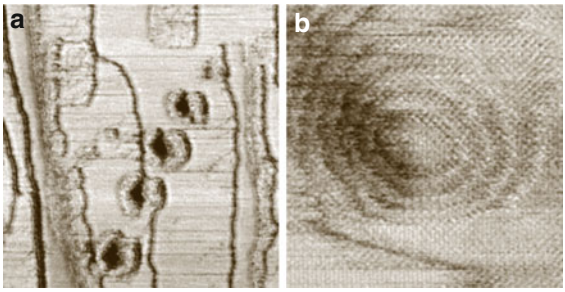

Fig. 15.38 **(a)** Lateral force images of the pits produced with $F_N = 5.7$–22.8 nN. Frame size: 150 nm; **(b)** Detailed image of the fourth pit from the top with pseudo-atomic resolution. Frame size: 20 nm

Although it is not that easy to understand how wear is initiated and how the tip transports the debris, important indications are given by the profile of the lateral force F_L recorded while scratching. Figure 15.37 shows some friction loops acquired when the tip was scanned laterally on areas of size 5×5 nm^2. The mean lateral force multiplied by the scanned length gives the total energy dissipated in the process. The tip movement produces the pits shown in Fig. 15.38a. Thanks to the pseudo-atomic resolution obtained by FFM (Fig. 15.38b), the number of removed atoms can be determined from lateral force images, which allow us to estimate that 70% of the dissipated energy went into wearless friction [88].

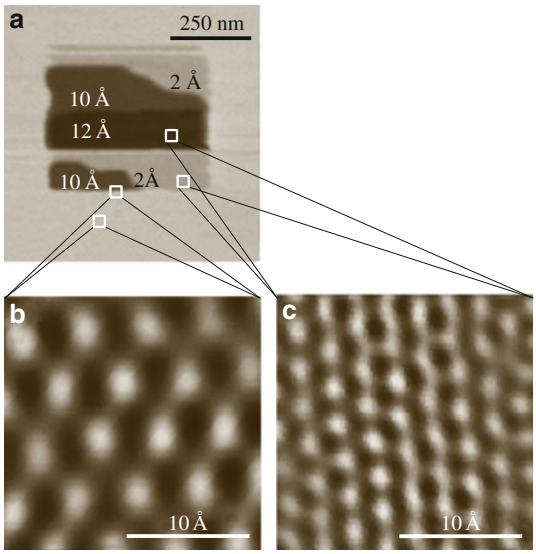

Fig. 15.39 **(a)** Topography image of an area scratched on muscovite mica with $F_N = 230$ nN; **(b, c)** Fourier-filtered images of different regions (after [89])

Figures 15.37 and 15.38 clearly show that the damage increases with increasing load. On the other hand, changing the scan velocity v between 25 and 100 nm/s did not produce any significant variation in the wear process.

In a recent study on KBr films on Cu(100) Filleter et al. [41] reported significant wear at intrinsic step edges of the films, where atomic coordination is lower. In contrast, low friction and no wear were observed across metal steps covered by KBr, which indicates a stabilizing effect of the alkali halide coating on the metal surface. A different kind of wear was observed on layered materials. Kopta et al. [89] removed layers from a muscovite mica surface by scratching with normal force $F_N = 230$ nN (Fig. 15.39a). Fourier-filtered images acquired on very small areas revealed the different periodicities of the underlying layers, which reflect the complex structure of the muscovite mica (Fig. 15.39b, c).

15.6.2 Contribution of Wear to Friction

The mean lateral force detected while scratching a KBr(100) surface with a fixed load $F_N = 11$ nN is shown in Fig. 15.40. A rather continuous increase in *friction* with the number of scratches N is observed, which can be approximated with the following exponential law

$$F_L = F_0 e^{-N/N_0} + F_\infty \left(1 - e^{-N/N_0}\right). \tag{15.39}$$

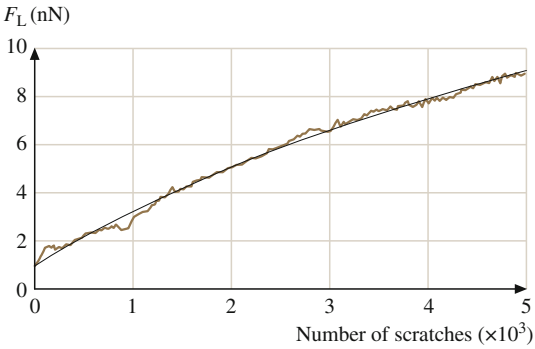

Fig. 15.40 Mean value of the lateral force during repeated scratching with $F_N = 11$ nN on a 500 nm line (after [88])

Equation (15.39) is easily interpreted by assuming that friction is proportional to contact area $A(N)$, and that time evolution of $A(N)$ can be described by

$$\frac{dA}{dN} = \frac{A_\infty - A(N)}{N_0}. \tag{15.40}$$

Here A_∞ is the limit area in which the applied load can be balanced without scratching.

To interpret their experiment on mica, Kopta et al. assumed that wear is initiated by atomic defects. When the defects accumulate beyond a critical concentration, they grow to form the scars shown in Fig. 15.39. Such a process was once again related to thermal activation. The number of defects created in the contact area $A(F_N)$ is

$$N_{def}(F_N) = t_{res} n_0 A(F_N) f_0 \exp\left(-\frac{\Delta E}{k_B T}\right), \tag{15.41}$$

where t_{res} is the residence time of the tip, n_0 is the surface density of atoms, and f_0 is the frequency of attempts to overcome the energy barrier ΔE to break a Si–O bond, which depends on the applied load. When the defect density reaches a critical value, a hole is nucleated. The friction force during the creation of a hole was also estimated via thermal activation by Kopta et al., who derived the formula

$$F_L = c(F_N - F_{off})^{\frac{2}{3}} + \gamma F_N^{\frac{2}{3}} \exp\left(B_0 F_N^{\frac{2}{3}}\right). \tag{15.42}$$

The first term on the right gives the wearless dependence of friction in the Hertz-plus-offset model (Sect. 15.5.1); the second term is the contribution of the defect production. The agreement between (15.42) and experiment can be observed in Fig. 15.41.

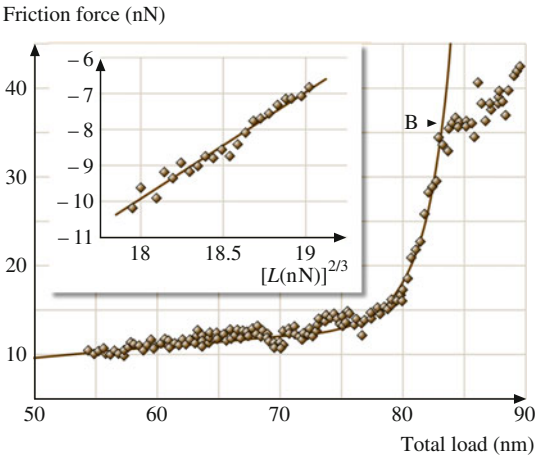

Fig. 15.41 Friction versus load curve during the creation of a hole in the muscovite mica (after [89])

15.7 Molecular Dynamics Simulations of Atomic Friction and Wear

Section 15.5 mentioned that small sliding contacts can be modeled by continuum mechanics. This modeling has several limitations. The first and most obvious is that continuum mechanics cannot account for atomic-scale processes like atomic stick–slip. While this limit can be overcome by semiclassical descriptions like the Tomlinson model, one definite limit is the determination of contact stiffness for contacts with a radius of a few nanometers. Interpreting experimental results with the methods introduced in Sect. 15.5.3 regularly yields contact radii of atomic or even smaller size, in clear contradiction to the minimal contact size given by adhesion forces. Macroscopic quantities such as shear modulus or pressure fail to describe the mechanical behavior of these contacts. Microscopic modeling that includes the atomic structure of the contact is therefore required. This is usually achieved through a *molecular dynamics* (MD) simulation of the contact. In such simulations, the sliding contact is set up by boundaries of fixed atoms in relative motion and the atoms of the contact, which are allowed to relax their positions according to interactions between each pair of atoms. Methods of computer simulation used in tribology are discussed elsewhere in this book. In this section we will discuss simulations that can be directly compared to experimental results showing atomic friction processes. The major outcome of the simulations beyond the inclusion of the atomic structure is the importance of including displacement of atoms in order to correctly predict forces. Then we present simulation studies that include wear of the tip or the surface.

15.7.1 Molecular Dynamics Simulations of Friction Processes

The first experiments that exhibited the features of atomic friction were performed on layered materials, often graphite. A theoretical study of forces between an atomically sharp diamond tip and the graphite surface has been reported by Tang et al. [90]. The authors found that the forces were significantly dependent on distance. The strongest contrasts appeared at different distances for normal and lateral forces due to the strong displacement of surface atoms. The order of magnitude found in this study was one nanonewton, much less than in most experimental reports, which indicated that contact areas of far larger dimensions were realized in such experiments. Tang et al. determined that the distance dependence of the forces could even change the symmetrical appearance of the lateral forces observed. The experimental situation has also been studied in numerical simulations using a simplified one-atom potential for the tip–surface interaction but including the spring potential of the probing force sensor [43]. The motivation for these studies was the observation of a hexagonal pattern in the friction force, while the surface atoms of graphite are ordered in a honeycomb structure. The simulations revealed how the jump path of the tip under lateral force is dependent on the force constant of the probing force sensor.

Surfaces of ionic crystals have become model systems for studies in atomic friction. Atomic stick–slip behavior has been observed by several groups with a lateral force modulation of the order of 1 nN. Pioneering work in atomistic simulation of sliding contacts has been done by Landman et al. The first ionic system studied was a CaF_2 tip sliding over a $CaF_2(111)$ surface [91]. In MD calculations with controlled temperature, the tip was first moved toward the surface up to the point at which an attractive normal force of -3 nN acted on the tip. Then the tip was moved laterally, and the lateral force determined. An oscillation with a periodicity corresponding to the atomic periodicity of the surface and with an amplitude decreasing from 8 nN was found. Inspection of the atomic positions revealed a wear process from shear cleavage of the tip. This transfer of atoms between tip and surface plays a crucial role in atomic friction studies, as was shown by Shluger et al. [92]. These authors simulated a MgO tip scanning laterally over a LiF(100) surface. Initially an irregular oscillation of the system's energy is found together with transfer of atoms between surface and tip. After a while, the tip apex structure is changed by adsorption of Li and F ions in such a way that nondestructive sliding with perfectly regular energy oscillations correlating with the periodicity of the surface was observed. The authors called this effect self-lubrication and speculate that, in general, dynamic self-organization of the surface material on the tip might promote the observation of periodic forces. In a less costly molecular mechanics study, in which the forces were calculated for each fixed tip–sample configuration, Tang et al. produced lateral and normal force maps for a diamond tip over a NaCl(100) surface, including such defects as vacancies and a step [93]. As with the studies mentioned before, they found that significant atomic force contrast can be expected for tip–sample distances of < 0.35 nm, while distances <0.15 nm

result in destructive forces. For the idealized conditions of scanning at constant height in this regime, the authors predict that even atomic-sized defects could be imaged. Experimentally, these conditions cannot be stabilized in the static modes used so far in lateral force measurements. However, dynamic modes of force microscopy have given atomic resolution of defects within the distance regime of 0.2 and 0.4 nm [94]. Recent experimental progress in atomic friction studies of surfaces of ionic crystals include the velocity dependence of lateral forces and atomic-scale wear processes. Such phenomena are not yet accessible by MD studies: the experimental scanning timescale is too far from the atomic relaxation timescales that govern MD simulations. Furthermore, the number of freely transferable atoms that can be included in a simulation is simply limited by meaningful calculation time.

Landman et al. also simulated a system of high reactivity, namely a silicon tip sliding over a silicon surface [95]. A clear stick–slip variation in the lateral force was observed for this situation. Strong atom displacements created an interstitial atom under the influence of the tip, which was annealed as the tip moved on. Permanent damage was predicted, however, when the tip enters the repulsive force regime. Although the simulated Si(111) surface is not experimentally accessible, it should be mentioned that the tip had to be passivated by a Teflon layer on the Si(111)-7 $\times$ 7 reconstructed surface before nondestructive contact mode measurements became possible (Sect. 15.3). It is worth noting that the simulations for the Cu(111) surface revealed a linear relation between contact area and mean lateral force, similar to classical macroscopic laws.

Wear processes are predicted by several MD studies of metallic sliding over metallic surfaces, which will be discussed in the following section. For a (111)-terminated copper tip sliding over a Cu(111) surface, however, Sørensen et al. found that nondestructive sliding is possible while the lateral force exhibits the sawtooth-like shape characteristic of atomic stick–slip (Fig. 15.42). In contrast, a Cu(100) surface would be disordered by a sliding contact (Fig. 15.43).

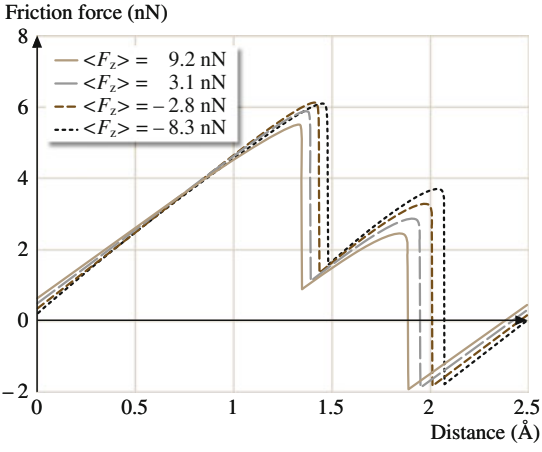

Fig. 15.42 Lateral force acting on a Cu(111) tip in matching contact with a Cu(111) substrate as a function of the sliding distance at different loads (after [96])

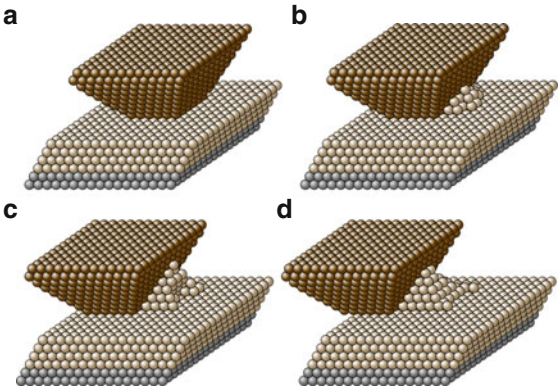

Fig. 15.43 Snapshot of a Cu(100) tip on a Cu(100) substrate during sliding. **(a)** Starting configuration; **(b–d)** snapshots after two, four, and six slips (after [96])

15.7.2 Molecular Dynamics Simulations of Abrasive Wear

The long timescales characteristic of wear processes and the large amount of material involved make any attempt to simulate these mechanisms on a computer a tremendous challenge. Despite this, MD can provide useful insights on the mechanisms of removal and deposition of single atoms by the FFM tip, which is not the kind of information directly observable experimentally. Complex processes like abrasive wear and nanolithography can be investigated only within approximate classical mechanics.

The observation made by Livshits and Shluger, that the FFM tip undergoes a process of self-lubrication when scanning ionic surfaces (Sect. 15.7.1), proves that friction and wear are strictly related phenomena. In their MD simulations on copper, Sørensen et al. considered not only ordered (111)- and (100)-terminated tips, but also amorphous structures obtained by *heating* the tip to high temperatures [96]. The lateral motion of the neck thus formed revealed stick–slip behavior due to combined sliding and stretching, as well as ruptures, accompanied by deposition of debris on the surface (Fig. 15.44).

To our knowledge, only a few examples of abrasive wear simulations on the atomic scale have been reported. Buldum and Ciraci, for instance, studied nanoindentation and sliding of a sharp Ni(111) tip on Cu(110) and a blunt Ni(001) tip on Cu(100) [97]. In the case of the sharp tip, quasiperiodic variations of the lateral force were observed, due to stick–slip involving phase transition. One layer of the asperity was deformed to match the substrate during the first slip and then two asperity layers merged into one in a structural transition during the second slip. In the case of the blunt tip, the stick–slip was less regular.

Different results have been reported in which the tip is harder than the underlying sample. Komanduri et al. considered an infinitely hard Ni indenter scratching single crystal aluminum at extremely low depths (Fig. 15.45) [98]. A linear relation between friction and load was found, with a high coefficient of friction $\mu = 0.6$, independent of the scratch depth. Nanolithography simulations were recently

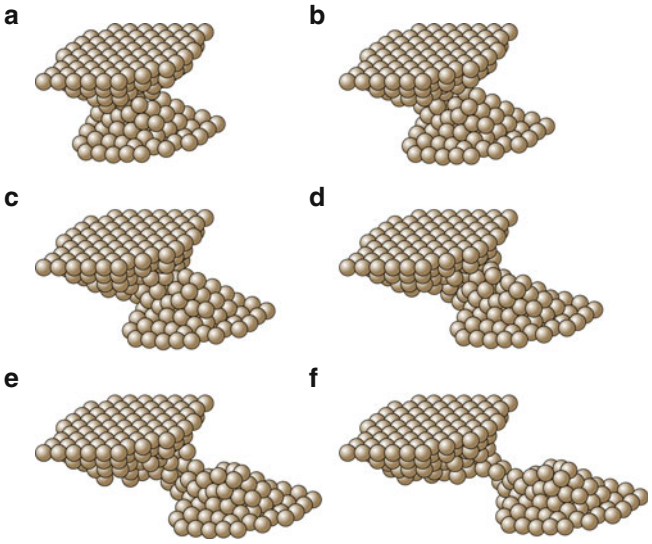

Fig. 15.44 Snapshot of a Cu(100) neck during shearing starting from configuration **(a)**. The upper substrate was displaced 4.2 Å between subsequent pictures (after [96])

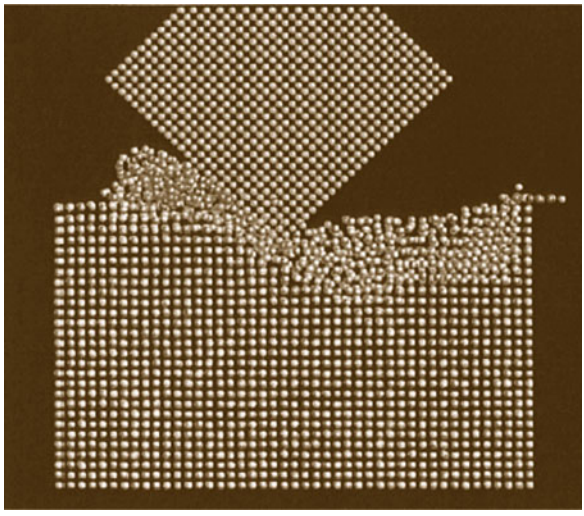

Fig. 15.45 MD simulation of a scratch realized with an infinitely hard tool (after [98])

performed by Fang et al. [99], who investigated the role of the displacement of the FFM tip along the direction of slow motion between a scan line and the next one. They found a certain correlation with FFM experiments on silicon films coated with aluminum.

15.8 Energy Dissipation in Noncontact Atomic Force Microscopy

Historically, the measurement of energy dissipation induced by tip–sample interaction has been the domain of friction force microscopy, where the sharp AFM tip slides over a sample that it is in gentle contact with. The origins of dissipation in friction are related to phonon excitation, electronic excitation and irreversible changes of the surface. In a typical stick–slip experiment, the energy dissipated in a single atomic slip event is of the order of 1 eV.

However, the lateral resolution of force microscopy in the contact mode is limited by a minimum contact area of several atoms due to adhesion between tip and sample.

This problem has been overcome in noncontact dynamic force microscopy. In the dynamic mode, the tip oscillates with a constant amplitude A of typically 1–20 nm at the eigenfrequency f of the cantilever, which shifts by Δf due to interaction forces between tip and sample. This technique is described in detail in Part B of this book.

Dissipation also occurs in the noncontact mode of force microscopy, where the atomic structure of tip and sample are reliably preserved. In this dynamic mode, the damping of the cantilever oscillation can be deduced from the excitation amplitude A_{exc} required to maintain the constant tip oscillation amplitude on resonance.

Compared to friction force microscopy, the interpretation of noncontact AFM (NC-AFM) experiments is complicated due to the perpendicular oscillation of the tip, typically with an amplitude that is large compared to the minimum tip–sample separation. Another problem is to relate the measured damping of the cantilever to the different origins of dissipation.

In all dynamic force microscopy measurements, a power dissipation P_0 caused by internal friction of the freely oscillating cantilever is observed, which is proportional to the eigenfrequency ω_0 and to the square of the amplitude A and is inversely proportional to the known Q value of the cantilever. When the tip–sample distance is reduced, the tip interacts with the sample and therefore additional damping of the oscillation is encountered. This extra dissipation P_{ts} caused by the tip–sample interaction can be calculated from the excitation signal A_{exc} [100].

The observed energy losses per oscillation cycle (100 meV) [101] are roughly similar to the 1 eV energy loss in the contact slip process. When estimating the contact area in the contact mode for a few atoms, the energy dissipation per atom that can be associated with a bond being broken and reformed is also $\approx$100 meV.

The idea of relating the additional damping of the tip oscillation to dissipative tip–sample interactions has recently attracted much attention [102]. The origins of this additional dissipation are manifold: one may distinguish between apparent energy dissipation (for example from inharmonic cantilever motion, artefacts from the phase controller, or slow fluctuations round the steady state solution [102, 103]), velocity-dependent dissipation (for example electric and magneticfield-mediated

Joule dissipation [104, 105]) and hysteresis-related dissipation (due to atomic instabilities [106, 107] or hysteresis due to adhesion [108]).

Forces and dissipation can be measured by recording Δf and A_{exc} simultaneously during a typical AFM experiment. Many experiments show true atomic contrast in topography (controlled by Δf) and in the dissipation signal A_{exc} [109]; however, the origin of the atomic energy dissipation process is still not completely resolved.

To prove that the observed atomic-scale variation in the damping is indeed due to atomic-scale energy dissipation and not an artefact of the distance feedback, Loppacher et al. [101] carried out a NC-AFM experiment on Si(111)-7 $\times$ 7 at constant height (with distance feedback stopped). Frequency-shift and dissipation exhibit atomic-scale contrast, demonstrating true atomic-scale variations in force and dissipation.

Strong atomic-scale dissipation contrast at step edges has been demonstrated in a few experiments (NaCl on Cu [94] or measurements on KBr [110]). In Fig. 15.46, ultrathin NaCl islands grown on Cu(111) are shown. As shown in Fig. 15.46a, the island edges have a higher contrast than the NaCl terrace and they show atomically resolved corrugation. The strongly enhanced contrast of the step edges and kink sites could be attributed to a slower decay of the electric field and to easier relaxation of the positions of the ions at these locations. The dissipation image shown in Fig. 15.46b was recorded at the same time. To establish a direct spatial correspondence between the excitation and the topography signal, the match between topography and A_{exc} has been studied on many images. Sometimes the topography and A_{exc} are in phase, sometimes they are shifted a little bit, and sometimes A_{exc} is at a minimum when topography is at a maximum. The local contrast formation thus depends strongly on the atomic tip structure. In fact, the strong dependence of the dissipation contrast on the atomic state of the tip apex is impressively confirmed by the tip change observed in the experimental images shown in Fig. 15.46b. The dissipation contrast is seriously enhanced, while the topography contrast remains almost unchanged. The dissipation clearly depends

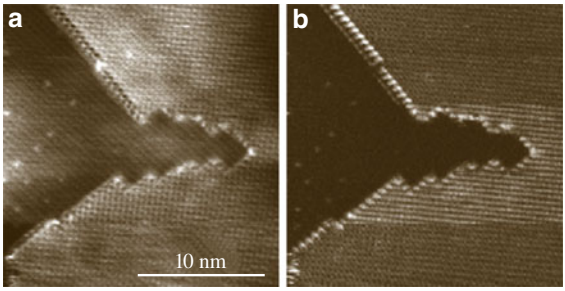

Fig. 15.46 **(a)** Topography and **(b)** A_{exc} images of a NaCl island on Cu(111). The tip changes after 1/4 of the scan, thereby changing the contrast in the topography and enhancing the contrast in A_{exc}. After 2/3 of the scan, the contrast from the *lower part* of the image is reproduced, indicating that the tip change was reversible (after [94])

strongly on the state of the tip and exhibits more short-range character than the frequency shift.

More directly related to friction measurements, where the tip is sliding in contact with the sample, are NC-AFM experiments, where the tip is oscillating parallel to the surface. Stowe et al. [111] oriented cantilever beams with in-plane tips perpendicular to the surface, so that the tip motion was approximately parallel to the surface. The noncontact damping of the lever was used to measure localized electrical Joule dissipation. They were able to image the dopant density for n- and p-type silicon samples with 150 nm spatial resolution. A dependence of U_{ts}^2 on the tip–sample voltage was found for the dissipation, as proposed by Denk and Pohl [104] for electric field Joule dissipation.

Stipe et al. [112] measured the noncontact friction between a Au(111) surface and a gold-coated tip with the same setup. They observed the same U_{ts}^2 dependence of the bias voltage and a distance dependence that follows the power law $1/d^n$, where n is between 1.3 and 3 [112, 113]. A substantial electric-field is present even when the external bias voltage is zero. The presence of inhomogeneous tip–sample electric fields is difficult to avoid, even under the best experimental conditions. Although this dissipation is electrical in origin, the detailed mechanism is not totally clear. The most straightforward mechanism is to assume that inhomogeneous fields emanating from the tip and the sample induce surface charges in the nearby metallic sample. When the tip moves, currents are induced, causing ohmic dissipation [104, 111]. But in metals with good electrical conductivity, ohmic dissipation is insufficient to account for the observed effect [114]. Thus the tip–sample electric field must have an additional effect, such as driving the motions of adsorbates and surface defects.

When exciting the torsional oscillation of commercial, rectangular AFM cantilevers, the tip is oscillating approximately parallel to the surface. In this mode, it was possible to measure lateral forces acting on the tip at step edges and near impurities quantitatively [65]. Enhanced energy dissipation was also observed at the impurities. When the tip is moved further toward the sample, contact formation transforms the nearly free torsional oscillation of the cantilever into a different mode, with the tip–sample contact acting as a hinge. When this contact is formed, a rapid increase in the power required to maintain a constant tip oscillation amplitude and a positive frequency shift are found. The onsets of the simultaneously recorded damping and positive frequency shift are sharp and essentially coincide. It is assumed that these changes indicate the formation of a tip–sample contact. Two recent studies [115, 116] report on the use of the torsional eigenmode to measure the elastic properties of the tip–sample contact, where the tip is in contact with the sample and the shear stiffness depends on the normal load.

Kawagishi et al. [117] scanned with lateral amplitudes of the order of 10 pm to 3 nm; their imaging technique showed up contrast between graphite terraces, silicon and silicon dioxide, graphite and mica. Torsional self-excitation showed nanometric features of self-assembled monolayer islands due to different lateral dissipations.

Giessibl et al. [118] recently established true atomic resolution of both conservative and dissipative forces by lateral force microscopy. The interaction between a single tip atom oscillated parallel to an Si(111)-7 × 7 surface was measured. A dissipation energy of up to 4 eV per oscillation cycle was found, which is explained by the plucking action of one atom onto the other, as described by Tomlinson in 1929 [25].

A detailed review of dissipation phenomena in noncontact force microscopy has been given by Hug [119].

15.9 Conclusion

Over the last 15 years, two instrumental developments have stimulated scientific activities in the field of nanotribology. On the one hand, the invention and development of friction force microscopy has allowed us to quantitatively study single-asperity friction. As we have discussed in this chapter, atomic processes are observed using forces of ≈1 nN (forces related to single chemical bonds). On the other hand, the enormous increase in achievable computing power has provided the basis for molecular dynamics simulations of systems containing several hundreds of atoms. These methods allow the development of the atomic structure in a sliding contact to be analyzed and the forces to be predicted.

The most prominent observation of atomic friction is stick–slip behavior with the periodicity of the surface atomic lattice. Semiclassical models can explain experimental findings, including the velocity dependence, which is a consequence of the thermal activation of slip events. Classical continuum mechanics can also describe the load dependence of friction in contacts with an extension of several tens of nanometers. However, when we try to apply continuum mechanics to contacts formed at just ten atoms, obviously wrong numbers result (for the contact radius for instance). Only comparison with atomistic simulations can provide a full, meaningful picture of the physical parameters of such sliding contacts. These simulations predict a close connection between wear and friction, in particular the transfer of atoms between surface and tip, which in some cases can even lower the friction in a process of self-lubrication.

First experiments have succeeded in studying the onset of wear with atomic resolution. Research into microscopic wear processes will certainly grow in importance as nanostructures are produced and their mechanical properties exploited. Simulations of such processes involving the transfer of thousands of atoms will become feasible with further increases in computing power. Another aspect of nanotribology is the expansion of atomic friction experiments toward surfaces with well-defined roughnesses. In general, the problem of bridging the gap between single-asperity experiments on well-defined surfaces and macroscopic friction should be approached, both experimentally and via modeling.

References

1. C.M. Mate, G.M. McClelland, R. Erlandsson, S. Chiang, Atomic-scale friction of a tungsten tip on a graphite surface. Phys. Rev. Lett. **59**, 1942–1945 (1987)
2. G. Binnig, C.F. Quate, C. Gerber, Atomic force microscope. Phys. Rev. Lett. **56**, 930–933 (1986)
3. O. Marti, J. Colchero, J. Mlynek, Combined scanning force and friction microscopy of mica. Nanotechnology **1**, 141–144 (1990)
4. G. Meyer, N. Amer, Simultaneous measurement of lateral and normal forces with an optical-beam-deflection atomic force microscope. Appl. Phys. Lett. **57**, 2089–2091 (1990)
5. G. Neubauer, S.R. Cohen, G.M. McClelland, D.E. Horn, C.M. Mate, Force microscopy with a bidirectional capacitance sensor. Rev. Sci. Instrum. **61**, 2296–2308 (1990)
6. G.M. McClelland, J.N. Glosli, Friction at the atomic scale. In: *NATO ASI Series E*, Vol. 220, ed. by L. Singer, H.M. Pollock (Kluwer, Dordrecht, 1992), pp. 405–425
7. R. Linnemann, T. Gotszalk, I.W. Rangelow, P. Dumania, E. Oesterschulze, Atomic force microscopy and lateral force microscopy using piezoresistive cantilevers. J. Vac. Sci. Technol. B **14**, 856–860 (1996)
8. M. Nonnenmacher, J. Greschner, O. Wolter, R. Kassing, Scanning force microscopy with micromachined silicon sensors. J. Vac. Sci. Technol. B **9**, 1358–1362 (1991)
9. R. Lüthi, Untersuchungen zur Nanotribologie und zur Auflösungsgrenze im Ultrahochvakuum mittels Rasterkraftmikroskopie. Ph.D. Thesis (University of Basel, Basel 1996)
10. J. Cleveland, S. Manne, D. Bocek, P.K. Hansma, A nondestructive method for determining the spring constant of cantilevers for scanning force microscopy. Rev. Sci. Instrum. **64**, 403–405 (1993)
11. J.L. Hutter, J. Bechhoefer, Calibration of atomic-force microscope tips. Rev. Sci. Instrum. **64**, 1868–1873 (1993)
12. H.J. Butt, M. Jaschke, Calculation of thermal noise in atomic-force microscopy. Nanotechnology **6**, 1–7 (1995)
13. J.M. Neumeister, W.A. Ducker, Lateral, normal, and longitudinal spring constants of atomic-force microscopy cantilevers. Rev. Sci. Instrum. **65**, 2527–2531 (1994)
14. D.F. Ogletree, R.W. Carpick, M. Salmeron, Calibration of frictional forces in atomic force microscopy. Rev. Sci. Instrum. **67**, 3298–3306 (1996)
15. E. Gnecco, AFM study of friction phenomena on the nanometer scale. Ph.D. Thesis (University of Genova, Genova, 2001)
16. U.D. Schwarz, P. Köster, R. Wiesendanger, Quantitative analysis of lateral force microscopy experiments. Rev. Sci. Instrum. **67**, 2560–2567 (1996)
17. J.E. Sader, C.P. Green, In-plane deformation of cantilever plates with applications to lateral force microscopy. Rev. Sci. Instrum. **75**, 878–883 (2004)
18. S.A. Edwards, W.A. Ducker, J.E. Sader, Influence of atomic force microscope cantilever tilt and induced torque on force measurements. J. Appl. Phys. **103**, 064513 (2008)
19. E. Meyer, R. Lüthi, L. Howald, M. Bammerlin, M. Guggisberg, H.-J. Güntherodt, Site-specific friction force spectroscopy. J. Vac. Sci. Technol. B **14**, 1285–1288 (1996)
20. S.S. Sheiko, M. Möller, E.M.C.M. Reuvekamp, H.W. Zandberger, Calibration and evaluation of scanning-force microscopy probes. Phys. Rev. B **48**, 5675 (1993)
21. F. Atamny, A. Baiker, Direct imaging of the tip shape by AFM. Surf. Sci. **323**, L314 (1995)
22. J.S. Villarrubia, Algorithms for scanned probe microscope image simulation, surface reconstruction, and tip estimation. J. Res. Natl. Inst. Stand. Technol. **102**, 425–454 (1997)
23. L. Howald, E. Meyer, R. Lüthi, H. Haefke, R. Overney, H. Rudin, H.-J. Güntherodt, Multifunctional probe microscope for facile operation in ultrahigh vacuum. Appl. Phys. Lett. **63**, 117–119 (1993)
24. Q. Dai, R. Vollmer, R.W. Carpick, D.F. Ogletree, M. Salmeron, A variable temperature ultrahigh vacuum atomic force microscope. Rev. Sci. Instrum. **66**, 5266–5271 (1995)
25. G.A. Tomlinson, A molecular theory of friction. Philos. Mag. Ser. **7**, 905 (1929)

26. T. Gyalog, M. Bammerlin, R. Lüthi, E. Meyer, H. Thomas, Mechanism of atomic friction. Europhys. Lett. **31**, 269–274 (1995)
27. T. Gyalog, H. Thomas, Friction between atomically flat surfaces. Europhys. Lett. **37**, 195–200 (1997)
28. M. Weiss, F.J. Elmer, Dry friction in the Frenkel–Kontorova–Tomlinson model:Static properties. Phys. Rev. B **53**, 7539–7549 (1996)
29. M.H. Müser, Structural lubricity: Role of dimension and symmetry. Europhys. Lett. **66**, 97 (2004)
30. J.B. Pethica, Comment on "Interatomic forces in scanning tunneling microscopy, Giant corrugations of the graphite surface". Phys. Rev. Lett. **57**, 3235 (1986)
31. E. Meyer, R.M. Overney, K. Dransfeld, T. Gyalog, *Nanoscience, Friction and Rheology on the Nanometer Scale* (World Scientific, Singapore, 1998)
32. A. Socoliuc, R. Bennewitz, E. Gnecco, E. Meyer, Transition from stick-slip to continuous sliding in atomic friction: Entering a new regime of ultralow friction. Phys. Rev. Lett. **92**, 134301 (2004)
33. A. Socoliuc, E. Gnecco, S. Maier, O. Pfeiffer, A. Baratoff, R. Bennewitz, E. Meyer, Atomic-scale control of friction by actuation of nanometer-sized contacts. Science **313**, 207–210 (2006)
34. R. Lüthi, E. Meyer, M. Bammerlin, L. Howald, H. Haefke, T. Lehmann, C. Loppacher, H.-J. Güntherodt, T. Gyalog, H. Thomas, Friction on the atomic scale: An ultrahigh vacuum atomic force microscopy study on ionic crystals. J. Vac. Sci. Technol. B **14**, 1280–1284 (1996)
35. S. Maier, E. Gnecco, A. Baratoff, R. Bennewitz, E. Meyer, Atomic scale friction modulated by a buried interface. Phys. Rev. B (2008), in press
36. S. Maier, Y. Sang, T. Filleter, M. Grant, R. Bennewitz, E. Gnecco, E. Meyer, Fluctuations and jump dynamics in atomic friction experiments. Phys. Rev. B **72**, 245418 (2008)
37. L. Howald, R. Lüthi, E. Meyer, H.-J. Güntherodt, Atomic-force microscopy on the Si(111) 7×7 surface. Phys. Rev. B **51**, 5484–5487 (1995)
38. R. Bennewitz, E. Gnecco, T. Gyalog, E. Meyer, Atomic friction studies on well-defined surfaces. Tribol. Lett. **10**, 51–56 (2001)
39. T. Filleter, W. Paul, R. Bennewitz, Atomic structure and friction of ultrathin films of KBr on Cu(100). Phys. Rev. B **77**, 035430 (2008)
40. G.J. Germann, S.R. Cohen, G. Neubauer, G.M. McClelland, H. Seki, Atomic-scale friction of a diamond tip on diamond (100) and (111) surfaces. J. Appl. Phys. **73**, 163–167 (1993)
41. R.J.A. van den Oetelaar, C.F.J. Flipse, Atomic-scale friction on diamond(111) studied by ultrahigh vacuum atomic force microscopy. Surf. Sci. **384**, L828–L835 (1997)
42. S. Fujisawa, E. Kishi, Y. Sugawara, S. Morita, Atomic-scale friction observed with a two-dimensional frictional-force microscope. Phys. Rev. B **51**, 7849–7857 (1995)
43. N. Sasaki, M. Kobayashi, M. Tsukada, Atomic-scale friction image of graphite in atomic-force microscopy. Phys. Rev. B **54**, 2138–2149 (1996)
44. H. Kawakatsu, T. Saito, Scanning force microscopy with two optical levers for detection of deformations of the cantilever. J. Vac. Sci. Technol. B **14**, 872–876 (1996)
45. M. Hirano, K. Shinjo, R. Kaneko, Y. Murata, Anisotropy of frictional forces in muscovite mica. Phys. Rev. Lett. **67**, 2642–2645 (1991)
46. M. Hirano, K. Shinjo, R. Kaneko, Y. Murata, Observation of superlubricity by scanning tunneling microscopy. Phys. Rev. Lett. **78**, 1448–1451 (1997)
47. R.M. Overney, H. Takano, M. Fujihira, W. Paulus, H. Ringsdorf, Anisotropy in friction and molecular stick-slip motion. Phys. Rev. Lett. **72**, 3546–3549 (1994)
48. H. Takano, M. Fujihira, Study of molecular scale friction on stearic acid crystals by friction force microscopy. J. Vac. Sci. Technol. B **14**, 1272–1275 (1996)
49. M. Dienwiebel, G. Verhoeven, N. Pradeep, J. Frenken, J. Heimberg, H. Zandbergen, Superlubricity of graphite. Phys. Rev. Lett. **92**, 126101 (2004)

50. M. Liley, D. Gourdon, D. Stamou, U. Meseth, T.M. Fischer, C. Lautz, H. Stahlberg, H. Vogel, N.A. Burnham, C. Duschl, Friction anisotropy and asymmetry of a compliant monolayer induced by a small molecular tilt. Science **280**, 273–275 (1998)
51. R. Lüthi, E. Meyer, H. Haefke, L. Howald, W. Gutmannsbauer, H.-J. Güntherodt, Sled-type motion on the nanometer scale: Determination of dissipation and cohesive energies of C_{60}. Science **266**, 1979–1981 (1994)
52. P.E. Sheehan, C.M. Lieber, Nanotribology and nanofabrication of MoO_3 structures by atomic force microscopy. Science **272**, 1158–1161 (1996)
53. M.R. Falvo, J. Steele, R.M. Taylor, R. Superfine, Evidence of commensurate contact and rolling motion: AFM manipulation studies of carbon nanotubes on HOPG. Tribol. Lett. **9**, 73–76 (2000)
54. E. Gnecco, R. Bennewitz, T. Gyalog, C. Loppacher, M. Bammerlin, E. Meyer, H.-J. Güntherodt, Velocity dependence of atomic friction. Phys. Rev. Lett. **84**, 1172–1175 (2000)
55. Y. Sang, M. Dubé, M. Grant, Thermal effects on atomic friction. Phys. Rev. Lett. **87**, 174301 (2001)
56. E. Riedo, E. Gnecco, R. Bennewitz, E. Meyer, H. Brune, Interaction potential and hopping dynamics governing sliding friction. Phys. Rev. Lett. **91**, 084502 (2003)
57. P. Reimann, M. Evstigneev, Nonmonotonic velocity dependence of atomic friction. Phys. Rev. Lett. **93**, 230802 (2004)
58. C. Fusco, A. Fasolino, Velocity dependence of atomic-scale friction: A comparative study of the one- and two-dimensional Tomlinson model. Phys. Rev. B **71**, 45413 (2005)
59. O. Zwörner, H. Hölscher, U.D. Schwarz, R. Wiesendanger, The velocity dependence of frictional forces in point-contact friction. Appl. Phys. A **66**, 263–267 (1998)
60. D. Gourdon, N.A. Burnham, A. Kulik, E. Dupas, F. Oulevey, G. Gremaud, D. Stamou, M. Liley, Z. Dienes, H. Vogel, C. Duschl, The dependence of friction anisotropies on the molecular organization of LB films as observed by AFM. Tribol. Lett. **3**, 317–324 (1997)
61. T. Bouhacina, J.P. Aimé, S. Gauthier, D. Michel, V. Heroguez, Tribological behavior of a polymer grafted on silanized silica probed with a nanotip. Phys. Rev. B **56**, 7694–7703 (1997)
62. H.J. Eyring, The activated complex in chemical reactions. J. Chem. Phys. **3**, 107 (1937)
63. J.N. Glosli, G.M. McClelland, Molecular dynamics study of sliding friction of ordered organic monolayers. Phys. Rev. Lett. **70**, 1960–1963 (1993)
64. R. Bennewitz, T. Gyalog, M. Guggisberg, M. Bammerlin, E. Meyer, H.-J. Güntherodt, Atomic-scale stick-slip processes on Cu(111). Phys. Rev. B **60**, R11301–R11304 (1999)
65. O. Pfeiffer, R. Bennewitz, A. Baratoff, E. Meyer, P. Grütter, Lateral-force measurements in dynamic force microscopy. Phys. Rev. B **65**, 161403 (2002)
66. E. Riedo, F. Lévy, H. Brune, Kinetics of capillary condensation in nanoscopic sliding friction. Phys. Rev. Lett. **88**, 185505 (2002)
67. M. He, A.S. Blum, G. Overney, R.M. Overney, Effect of interfacial liquid structuring on the coherence length in nanolubrucation. Phys. Rev. Lett. **88**, 154302 (2002)
68. A. Schirmeisen, L. Jansen, H. Hölscher, H. Fuchs, Temperature dependence of point contact friction on silicon. Appl. Phys. Lett. **88**, 123108 (2006)
69. X. Zhao, M. Hamilton, W.G. Sawyer, S.S. Perry, Thermally activated friction. Tribol. Lett. **27**, 113–117 (2007)
70. F.P. Bowden, F.P. Tabor, *The Friction and Lubrication of Solids* (Oxford University Press, Oxford, 1950)
71. L.D. Landau, E.M. Lifshitz, *Introduction to Theoretical Physics* (Nauka, Moscow, 1998), Vol. 7
72. J.A. Greenwood, J.B.P. Williamson, Contact of nominally flat surfaces. Proc. R. Soc. Lond. A **295**, 300 (1966)
73. B.N.J. Persson, Elastoplastic contact between randomly rough surfaces. Phys. Rev. Lett. **87**, 116101 (2001)

74. K.L. Johnson, K. Kendall, A.D. Roberts, Surface energy and contact of elastic solids. Proc. R. Soc. Lond. A **324**, 301 (1971)
75. B.V. Derjaguin, V.M. Muller, Y.P. Toporov, Effect of contact deformations on adhesion of particles. J. Colloid Interface Sci. **53**, 314–326 (1975)
76. D. Tabor, Surface forces and surface interactions. J. Colloid Interface Sci. **58**, 2–13 (1977)
77. D. Maugis, Adhesion of spheres, the JKR-DMT transition using a Dugdale model. J. Colloid Interface Sci. **150**, 243–269 (1992)
78. U.D. Schwarz, O. Zwörner, P. Köster, R. Wiesendanger, Quantitative analysis of the frictional properties of solid materials at low loads. Phys. Rev. B **56**, 6987–6996 (1997)
79. R.W. Carpick, N. Agraït, D.F. Ogletree, M. Salmeron, Measurement of interfacial shear (friction) with an ultrahigh vacuum atomic force microscope. J. Vac. Sci. Technol. B **14**, 1289–1295 (1996)
80. C. Polaczyk, T. Schneider, J. Schöfer, E. Santner, Microtribological behavior of Au(001) studied by AFM/FFM. Surf. Sci. **402**, 454–458 (1998)
81. J.N. Israelachvili, D. Tabor, Measurement of van der Waals dispersion forces in range 1.5 to 130 nm. Proc. R. Soc. Lond. A **331**, 19 (1972)
82. S.P. Jarvis, A. Oral, T.P. Weihs, J.B. Pethica, A novel force microscope and point-contact probe. Rev. Sci. Instrum. **64**, 3515–3520 (1993)
83. R.W. Carpick, D.F. Ogletree, M. Salmeron, Lateral stiffness: A new nanomechanical measurement for the determination of shear strengths with friction force microscopy. Appl. Phys. Lett. **70**, 1548–1550 (1997)
84. M.A. Lantz, S.J. O'Shea, M.E. Welland, K.L. Johnson, Atomic-force-microscope study of contact area and friction on $NbSe_2$. Phys. Rev. B **55**, 10776–10785 (1997)
85. K.L. Johnson, *Contact Mechanics* (Cambridge University Press, Cambridge 1985)
86. M. Enachescu, R.J.A. van den Oetelaar, R.W. Carpick, D.F. Ogletree, C.F.J. Flipse, M. Salmeron, Atomic force microscopy study of an ideally hard contact: the diamond (111)/tungsten carbide interface. Phys. Rev. Lett. **81**, 1877–1880 (1998)
87. M. Enachescu, R.J.A. van den Oetelaar, R.W. Carpick, D.F. Ogletree, C.F.J. Flipse, M. Salmeron, Observation of proportionality between friction and contact area at the nanometer scale. Tribol. Lett. **7**, 73–78 (1999)
88. E. Gnecco, R. Bennewitz, E. Meyer, Abrasive wear on the atomic scale. Phys. Rev. Lett. **88**, 215501 (2002)
89. S. Kopta, M. Salmeron, The atomic scale origin of wear on mica and its contribution to friction. J. Chem. Phys. **113**, 8249–8252 (2000)
90. H. Tang, C. Joachim, J. Devillers, Interpretation of AFM images – the graphite surface with a diamond tip. Surf. Sci. **291**, 439–450 (1993)
91. U. Landman, W.D. Luedtke, E.M. Ringer, Atomistic mechanisms of adhesive contact formation and interfacial processes. Wear **153**, 3–30 (1992)
92. A.I. Livshits, A.L. Shluger, Self-lubrication in scanning force microscope image formation on ionic surfaces. Phys. Rev. B **56**, 12482–12489 (1997)
93. H. Tang, X. Bouju, C. Joachim, C. Girard, J. Devillers, Theoretical study of the atomic-force microscopy imaging process on the NaCl(100) surface. J. Chem. Phys. **108**, 359–367 (1998)
94. R. Bennewitz, A.S. Foster, L.N. Kantorovich, M. Bammerlin, C. Loppacher, S. Schär, M. Guggisberg, E. Meyer, A.L. Shluger, Atomically resolved edges and kinks of NaCl islands on Cu(111): Experiment and theory. Phys. Rev. B **62**, 2074–2084 (2000)
95. U. Landman, W.D. Luetke, M.W. Ribarsky, Structural and dynamical consequences of interactions in interfacial systems. J. Vac. Sci. Technol. A **7**, 2829–2839 (1989)
96. M.R. Sørensen, K.W. Jacobsen, P. Stoltze, Simulations of atomic-scale sliding friction. Phys. Rev. B **53**, 2101–2113 (1996)
97. A. Buldum, C. Ciraci, Contact, nanoindentation and sliding friction. Phys. Rev. B **57**, 2468–2476 (1998)
98. R. Komanduri, N. Chandrasekaran, L.M. Raff, Molecular dynamics simulation of atomic-scale friction. Phys. Rev. B **61**, 14007–14019 (2000)

99. T.H. Fang, C.I. Weng, J.G. Chang, Molecular dynamics simulation of a nanolithography process using atomic force microscopy. Surf. Sci. **501**, 138–147 (2002)
100. B. Gotsmann, C. Seidel, B. Anczykowski, H. Fuchs, Conservative and dissipative tip–sample interaction forces probed with dynamic AFM. Phys. Rev. B **60**, 11051–11061 (1999)
101. C. Loppacher, R. Bennewitz, O. Pfeiffer, M. Guggisberg, M. Bammerlin, S. Schär, V. Barwich, A. Baratoff, E. Meyer, Experimental aspects of dissipation force microscopy. Phys. Rev. B **62**, 13674–13679 (2000)
102. M. Gauthier, M. Tsukada, Theory of noncontact dissipation force microscopy. Phys. Rev. B **60**, 11716–11722 (1999)
103. J.P. Aimé, R. Boisgard, L. Nony, G. Couturier, Nonlinear dynamic behavior of an oscillating tip-microlever system and contrast at the atomic scale. Phys. Rev. Lett. **82**, 3388–3391 (1999)
104. W. Denk, D.W. Pohl, Local electrical dissipation imaged by scanning force microscopy. Appl. Phys. Lett. **59**, 2171–2173 (1991)
105. S. Hirsekorn, U. Rabe, A. Boub, W. Arnold, On the contrast in eddy current microscopy using atomic force microscopes. Surf. Interf. Anal. **27**, 474–481 (1999)
106. U. Dürig, Atomic-Scale Metal Adhesion. In: *Forces in Scanning Probe Methods*, NATO ASI Ser. E, Vol. 286, ed. by H.J. Güntherodt, D. Anselmetti, E. Meyer (Kluwer, Dordrecht, 1995) pp. 191–234
107. N. Sasaki, M. Tsukada, Effect of microscopic nonconservative process on noncontact atomic force microscopy. Jpn. J. Appl. Phys. **39**, L1334–L1337 (2000)
108. B. Gotsmann, H. Fuchs, The measurement of hysteretic forces by dynamic AFM. Appl. Phys. A **72**, 55–58 (2001)
109. M. Guggisberg, M. Bammerlin, A. Baratoff, R. Lüthi, C. Loppacher, F.M. Battiston, J. Lü, R. Bennewitz, E. Meyer, H.J. Güntherodt, Dynamic force microscopy across steps on the Si (111)-(7 $\times$ 7) surface. Surf. Sci. **461**, 255–265 (2000)
110. R. Bennewitz, S. Schär, V. Barwich, O. Pfeiffer, E. Meyer, F. Krok, B. Such, J. Kolodzej, M. Szymonski, Atomic-resolution images of radiation damage in KBr. Surf. Sci. **474**, 197–202 (2001)
111. T.D. Stowe, T.W. Kenny, J. Thomson, D. Rugar, Silicon dopant imaging by dissipation force microscopy. Appl. Phys. Lett. **75**, 2785–2787 (1999)
112. B.C. Stipe, H.J. Mamin, T.D. Stowe, T.W. Kenny, D. Rugar, Noncontact friction and force fluctuations between closely spaced bodies. Phys. Rev. Lett. **87**, 96801 (2001)
113. B. Gotsmann, H. Fuchs, Dynamic force spectroscopy of conservative and dissipative forces in an Al-Au(111) tip–sample system. Phys. Rev. Lett. **86**, 2597–2600 (2001)
114. B.N.J. Persson, A.I. Volokitin, Comment on "Brownian motion of microscopic solids under the action of fluctuating electromagnetic fields". Phys. Rev. Lett. **84**, 3504 (2000)
115. K. Yamanaka, A. Noguchi, T. Tsuji, T. Koike, T. Goto, Quantitative material characterization by ultrasonic AFM. Surf. Interface Anal. **27**, 600–606 (1999)
116. T. Drobek, R.W. Stark, W.M. Heckl, Determination of shear stiffness based on thermal noise analysis in atomic force microscopy: Passive overtone microscopy. Phys. Rev. B **64**, 045401 (2001)
117. T. Kawagishi, A. Kato, Y. Hoshi, H. Kawakatsu, Mapping of lateral vibration of the tip in atomic force microscopy at the torsional resonance of the cantilever. Ultramicroscopy **91**, 37–48 (2002)
118. F.J. Giessibl, M. Herz, J. Mannhart, Friction traced to the single atom. Proc. Natl. Acad. Sci. USA **99**, 12006–12010 (2002)
119. H.-J. Hug, A. Baratoff, Measurement of dissipation induced by tip–sample interactions. In: *Noncontact Atomic Force Microscopy*, ed. by S. Morita, R. Wiesendanger, E. Meyer (Springer, Berlin, 2002), p. 395